Ataxin-3 phosphorylation decreases neuronal defects in spinocerebellar ataxia type 3 models

Carlos A. Matos,[1,2] Clévio Nóbrega,[1]* Susana R. Louros,[1]* Bruno Almeida,[3] Elisabete Ferreiro,[1,4] Jorge Valero,[1,5] Luís Pereira de Almeida,[1,6] Sandra Macedo-Ribeiro,[3] and Ana Luísa Carvalho[1,2]

[1]CNC - Center for Neuroscience and Cell Biology, University of Coimbra, 3004-504 Coimbra, Portugal
[2]Department of Life Sciences, Faculty of Sciences and Technology, University of Coimbra, 3004-517 Coimbra, Portugal
[3]Instituto de Biologia Molecular e Celular and Instituto de Investigação e Inovação em Saúde, University of Porto, 4200-135 Porto, Portugal
[4]Institute for Interdisciplinary Research, University of Coimbra, 3030-789 Coimbra, Portugal
[5]Ikerbasque Basque Foundation for Science and Achucarro Basque Center for Neuroscience, Bizkaia Science and Technology Park, E-48170 Zamudio, Spain
[6]Faculty of Pharmacy, University of Coimbra, 3000-548 Coimbra, Portugal

Different neurodegenerative diseases are caused by aberrant elongation of repeated glutamine sequences normally found in particular human proteins. Although the proteins involved are ubiquitously distributed in human tissues, toxicity targets only defined neuronal populations. Changes caused by an expanded polyglutamine protein are possibly influenced by endogenous cellular mechanisms, which may be harnessed to produce neuroprotection. Here, we show that ataxin-3, the protein involved in spinocerebellar ataxia type 3, also known as Machado-Joseph disease, causes dendritic and synapse loss in cultured neurons when expanded. We report that S12 of ataxin-3 is phosphorylated in neurons and that mutating this residue so as to mimic a constitutive phosphorylated state counters the neuromorphologic defects observed. In rats stereotaxically injected with expanded ataxin-3–encoding lentiviral vectors, mutation of serine 12 reduces aggregation, neuronal loss, and synapse loss. Our results suggest that S12 plays a role in the pathogenic pathways mediated by polyglutamine-expanded ataxin-3 and that phosphorylation of this residue protects against toxicity.

Introduction

Unrelated proteins containing glutamine repeat sequences are known to cause neurodegenerative disorders when the repeat-containing tracts are expanded beyond a critical threshold (Zoghbi and Orr, 2000). Pathogenesis of polyglutamine (polyQ) diseases is still poorly understood, but the fact that clinical presentation and neurodegeneration profiles do not overlap in these diseases indicates that the biologic specificities of each causative protein interfere with expansion-induced toxicity (Gatchel and Zoghbi, 2005). Machado-Joseph disease (MJD), otherwise known as spinocerebellar ataxia type 3, is one such disease and is recognized as the most common form of dominantly inherited ataxia in the world (Schöls et al., 2004; Bettencourt and Lima, 2011), involving the structural and functional compromise of discrete brain regions, such as the cerebellum, the pons, and the striatum (Alves et al., 2008b; Rüb et al., 2013).

MJD is caused by an abnormal expansion of a polyQ sequence contained in ataxin-3 (atx3; Kawaguchi et al., 1994), a protein of elusive biologic function nonetheless described as being involved in protein homeostasis systems, transcription regulation, and cytoskeleton organization (Matos et al., 2011). Atx3 displays deubiquitinase (DUB) activity, which is mediated by a catalytic triad of amino acids localized in a globular N-terminal Josephin domain (JD) that also includes two binding sites for ubiquitin (Ub; Mao et al., 2005; Nicastro et al., 2005, 2009). A flexible C-terminal tail comprises the polyQ tract and two or three ubiquitin-interacting motifs (UIMs), depending on the isoform (Harris et al., 2010).

PolyQ-expanded atx3 is known to cause cellular stress and to have an increased tendency to aggregate in vitro and in cultured cells, forming inclusions in MJD patients' brains often localized in cell nuclei (Paulson et al., 1997b; Zoghbi and Orr, 2000; Gales et al., 2005; Bauer and Nukina, 2009; Matos et al., 2011; Scarff et al., 2015). Contrastingly, atx3 is ubiquitously expressed in diverse tissues and cell types (Trottier et al., 1998; Bauer and Nukina, 2009), indicating that region-specific mechanisms of toxicity are responsible for the localized neurodegeneration. The fact that cell demise targets neurons specifically (Trottier et al., 1998; Rüb et al., 2013) suggests that atx3 may play an important role in neuronal cells, which is disturbed on

*C. Nóbrega and S.R. Louros contributed equally to this paper.

Correspondence to Ana Luísa Carvalho: alc@cnc.uc.pt

Abbreviations used in this paper: DIV, days in vitro; DUB, deubiquitinase; JD, Josephin domain; MJD, Machado-Joseph disease; polyQ, polyglutamine; PSD-95, postsynaptic density protein 95; Ub, ubiquitin; UIM, ubiquitin-interacting motif; VGLUT1, vesicular glutamate transporter subtype 1; WT, wild type.

Supplemental material can be found at:
http://doi.org/10.1083/jcb.201506025

The Rockefeller University Press $30.00
J. Cell Biol. Vol. 212 No. 4 465–480
www.jcb.org/cgi/doi/10.1083/jcb.201506025

polyQ expansion, but no function that would be specifically critical for neuronal survival or activity has ever been described.

The variable effects of polyQ-expanded atx3 in different cell types may result from diverging regulatory mechanisms of its properties and functions (Gatchel and Zoghbi, 2005; La Spada and Taylor, 2010; Takahashi et al., 2010). Tapping into these pathways constitutes a promising approach to the treatment of MJD. In cells, proteins are frequently regulated by posttranslational modifications (La Spada and Taylor, 2010; Takahashi et al., 2010) and among them phosphorylation has been repeatedly described to modulate the toxicity of polyQ disease–related proteins (Pennuto et al., 2009). For example, preventing expanded ataxin-1 phosphorylation at S776 renders the protein unable to form aggregates and ameliorates disease phenotype (Emamian et al., 2003). Contrastingly, phosphorylation of huntingtin at S421 decreases aggregation and cell death in cell culture models (Humbert et al., 2002; Luo et al., 2005); mimicking this modification by mutating S421 to aspartate is neuroprotective in a lentiviral rat model (Pardo et al., 2006).

To date, five atx3 phosphorylation sites have been described, all localized in the UIMs: S236 in the first UIM , S256 and 260/261 in the second, and S340 and 352 in the third UIM (Fei et al., 2007; Mueller et al., 2009). S256 is phosphorylated in vitro by glycogen synthase kinase 3β and preventing this modification enhances the aggregation of expanded atx3 (Fei et al., 2007). Simulating phosphorylation of S236, or S340 and S352 simultaneously, leads to an increased atx3 nuclear localization in cell lines and enhances repression of atx3-regulated transcription in gene reporter assays (Mueller et al., 2009). Pharmacologic inhibition of casein kinase 2, which was shown to phosphorylate atx3 C-terminal region, reduces the levels of nuclear atx3, activates atx3-regulated gene transcription, and decreases inclusion formation (Tao et al., 2008; Mueller et al., 2009).

We have observed that pathogenic expansion of atx3 causes a loss of dendrites and synapses in cultured neurons. Mimicking atx3 phosphorylation at S12, a novel phosphorylation site we hereby describe, reverts these effects, suggesting that atx3 may be functionally involved in the maintenance of these neuronal structures. Furthermore, we show that mutating S12 ameliorates aggregation, degeneration, and synapse loss in the brain of a MJD lentiviral rat model with striatal pathology (Pardo et al., 2006; Alves et al., 2008b), suggesting that phosphorylation at this residue may constitute a therapeutic target for MJD treatment.

Results

PolyQ-expanded atx3 causes dendrite and synapse loss in rat neuronal cultures

The cytotoxicity of polyQ-expanded atx3 is contingent on the cellular type in which the protein is being expressed, considering that only neurons are targeted in MJD (Zoghbi and Orr, 2000; Rüb et al., 2013). To determine if polyQ expansion of atx3 causes neuron-specific morphologic changes that may underlie impaired survival and function, we started by comparing the dendritic tree of rat neuron cultures expressing human atx3 with a pathogenic number of glutamines (84Q) or a nonpathogenic number of repeats (28Q). Cortical neurons, used considering the increasing evidence supporting the involvement of the cortex in the disease (Soong et al., 1997; Taniwaki et al., 1997; Murata et al., 1998; Ichikawa et al., 2001; Yamada et al., 2001; D'Abreu et al., 2012; Lopes et al., 2013; Pedroso et al., 2013; Rüb et al., 2013), were transfected with GFP-tagged human atx3 (Fig. 1 A), and the length of dendritic tracts of GFP-positive cells was measured. GFP-atx3 84Q-expressing neurons show a decreased total extension of dendrites, expressed as the sum of the length of all dendritic tracts in each cell (Fig. 1 B). Sholl analysis was used to evaluate dendrite complexity and further demonstrated that neurons expressing GFP-atx3 84Q display a withered dendritic tree, with less dendrites reaching 80–160 µm from the cell body and no dendrites reaching >170 µm (Fig. 1 C). This indicates that, in transfected cortical neurons, expansion of GFP-atx3 causes dendritic loss or shrinkage.

We then tested whether atx3 expansion affected synaptic contacts established between the cultured neurons. Visualization of functional excitatory glutamatergic synapses was achieved by colocalizing the punctuate signal of pre- and postsynaptic protein markers: the vesicular glutamate transporter subtype 1 (VGLUT1) and postsynaptic density protein 95 (PSD -95; Fig. 1 D). Compared with neurons transfected with GFP -atx3 28Q, neurons expressing GFP-atx3 84Q have a significant reduction in the number of glutamatergic synapses (Fig. 1 E). Similar differences were detected for inhibitory postsynaptic terminals, as evaluated by the number of gephyrin-positive puncta (Fig. 1, F and G).

Importantly, compared with neurons expressing the empty GFP vector, cells transfected with GFP-atx3 28Q show no differences in any of the parameters analyzed, underscoring the role of the polyQ expansion of GFP-atx3 in the phenotypes observed (Fig. S1). Results therefore indicate that polyQ expansion of atx3 in transfected cultured neurons causes morphologic defects in neuron-specific structures.

Atx3 is phosphorylated at S12 in mammalian neurons

We moved on to explore novel phosphorylation sites of atx3 that could account for the modulation of toxicity of the protein, starting by a mass spectrometry analysis directed at phosphorylation site detection. GFP-atx3 28Q was purified from transiently transfected HEK 293FT cells by immunoprecipitation and SDS-PAGE (Fig. 2 A), and peptides resulting from tryptic digestion of the GFP-atx3 bands were separated by reverse-phase high performance liquid chromatography and electrosprayed into the mass spectrometer. Examination of the protein sample produced from okadaic acid–stimulated cells revealed the presence of one phosphorylated peptide and mapped S12 as the modified residue (Fig. 2 B).

We then generated a phosphospecific antibody recognizing atx3 phosphorylated at S12 (anti-Patx3; Fig. 2 C) and used it to probe extracts from cultured rat cortical neurons. Western blot analysis yielded a band with the molecular weight expected of endogenous rat atx3 (Fig. 2 D), which is absent when the protein is knocked-down in cultures transduced with lentiviral vectors encoding atx3-targeting shRNAs (Alves et al., 2010). Bands of lower molecular weight yielded by the anti-Patx3 antibody possibly correspond to endogenous atx3-derived fragments mentioned in other studies (Berke et al., 2005; Pozzi et al., 2008; Koch et al., 2011; Simões et al., 2012). Higher molecular weight endogenous atx3 protein bands have also been observed in previous studies (Paulson et al., 1997a; Trottier et al., 1998; Koch et al., 2011). Neuronal extracts prepared in the absence of phosphatase inhibitors display decreased immunoreactivity, supporting that the

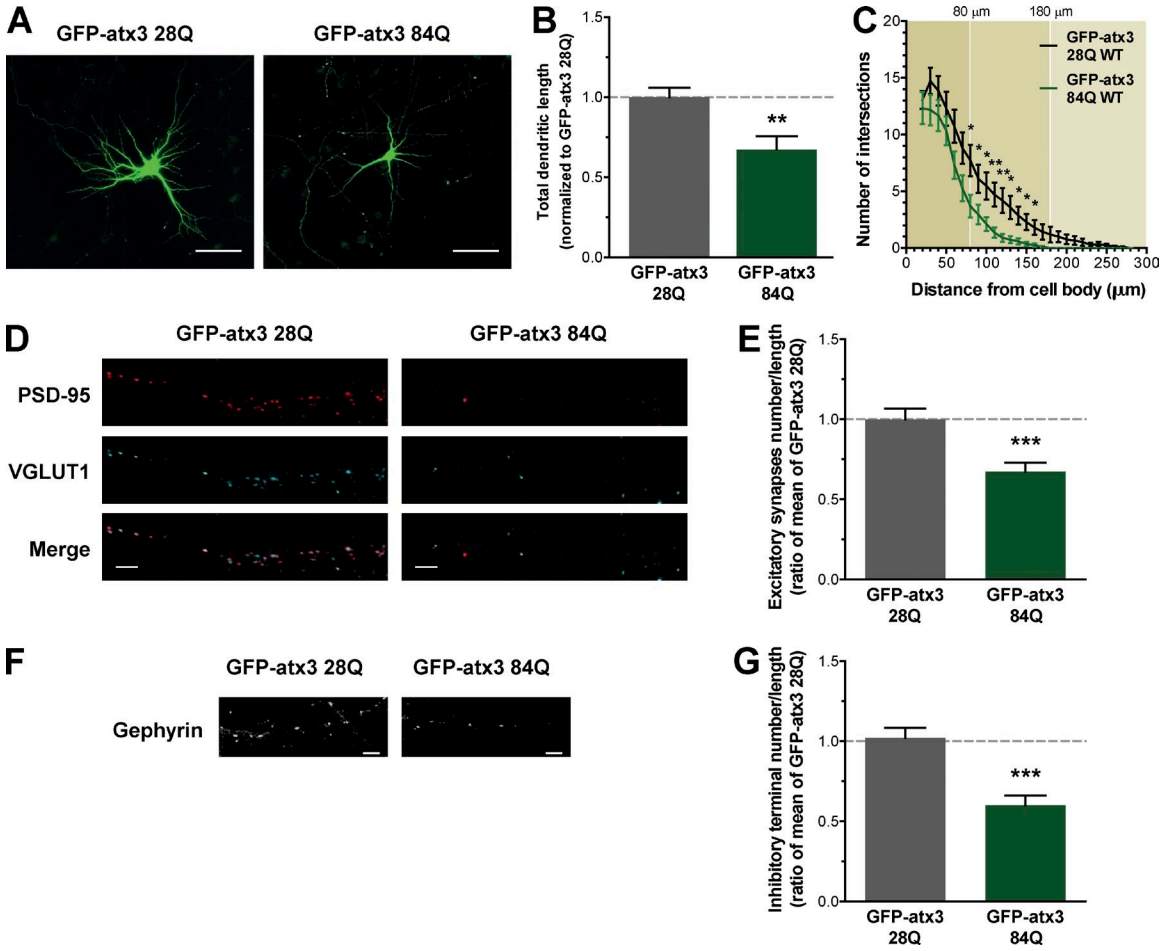

Figure 1. **PolyQ expansion of atx3 causes dendrite and synapse loss in cortical neurons.** (A) Rat cortical neuron cultures were transfected with nonexpanded GFP-atx3 28Q and expanded GFP-atx3 84Q. The panel shows representative fluorescence microscopy images of the cell body and dendritic tree. Bars, 100 µm. (B) Neurons expressing GFP-atx3 84Q WT display a reduced total length of dendritic tracts (n = 19–21, from two independent experiments; t test: **, $P < 0.01$). (C) Sholl analysis reveals a contraction of dendrites caused by GFP-atx3 84Q expression, comparing with neurons expressing GFP -atx3 28Q (n = 19–21 neurons, from two independent experiments; t test: *, $P < 0.05$; **, $P < 0.01$). (D) Excitatory synapses were immunocytochemically detected as instances of PSD-95 and VGLUT1 puncta colocalization (merge); (F) inhibitory postsynaptic terminals were quantified as gephyrin-positive puncta. Panels show representative fluorescence microscopy images of dendritic tracts evidencing synaptic marker puncta. Bars, 5 µm. (E and G) Expression of GFP-atx3 84Q causes a decrease in the number of excitatory synapses (n = 31–32 neurons, from three independent experiments; t test: ***, $P < 0.001$) and inhibitory postsynaptic terminals (n = 30–31 neurons, from three independent experiments; t test: ***, $P < 0.001$), compared with expression of GFP-atx3 28Q. (B, C, E, and G) Graph bars represent mean ± SEM.

anti-Patx3 antibody is labeling phosphorylated atx3 (Fig. 2 E). The analysis of Patx3 labeling in MJD patient's fibroblasts and in fibroblasts of a healthy control (Fig. 2, F and G) revealed a protein band pattern similar to that observed in cultured rat neurons, indicating that atx3 is phosphorylated in human samples.

Our observations indicate that S12 is a phosphorylation site of endogenous atx3 and that phosphate conjugation to this residue occurs normally in cultured rat neurons and human fibroblasts.

Mimicking S12 phosphorylation decreases atx3 DUB activity in vitro

S12 is localized in the catalytic JD (aa 8–168), the N-terminal domain of atx3 (Masino et al., 2003; Almeida et al., 2013; Fig. 3 A). In the solution structure of atx3 JD (Nicastro et al., 2005), S12 is located at the cleft between the globular catalytic subdomain and the flexible helical hairpin predicted to play a role in substrate recognition (Komander et al., 2009; Nicastro et al., 2009). S12 is located in the loop preceding helix α1, where C14, the nucleophile of the catalytic triad, is located, and nearby Q9, the residue proposed to contribute to the stabilization of the negatively charged transition state during peptide bond cleavage (Nicastro et al., 2005; Fig. 3 B). S12 is also adjacent to the loop centered on S72, which precedes the helical hairpin that comprises the docking site for the C terminus of the Ub substrate (Nicastro et al., 2009; Fig. 3, C and D). S12 is exposed to the solvent on the surface of the JD and is consequently accessible for phosphate conjugation. The proximity of S12 to structural elements associated to substrate binding and hydrolysis suggests that phosphorylation at this residue affects atx3 DUB activity.

We investigated the effect of S12 phosphorylation on atx3 enzymatic activity using in vitro DUB assays. A mutant of hexahistidine (6His)-atx3 with S12 substituted by a negatively charged aspartate, 6His-atx3 S12D, was generated to mimic constitutive phosphorylation. Because 6His-atx3 wild type (WT) and 6His-atx3 S12D were expressed in *Escherichia coli*, nonmutated His-atx3 WT is not phosphorylated. After purifying the proteins through a series of chromatographic steps as

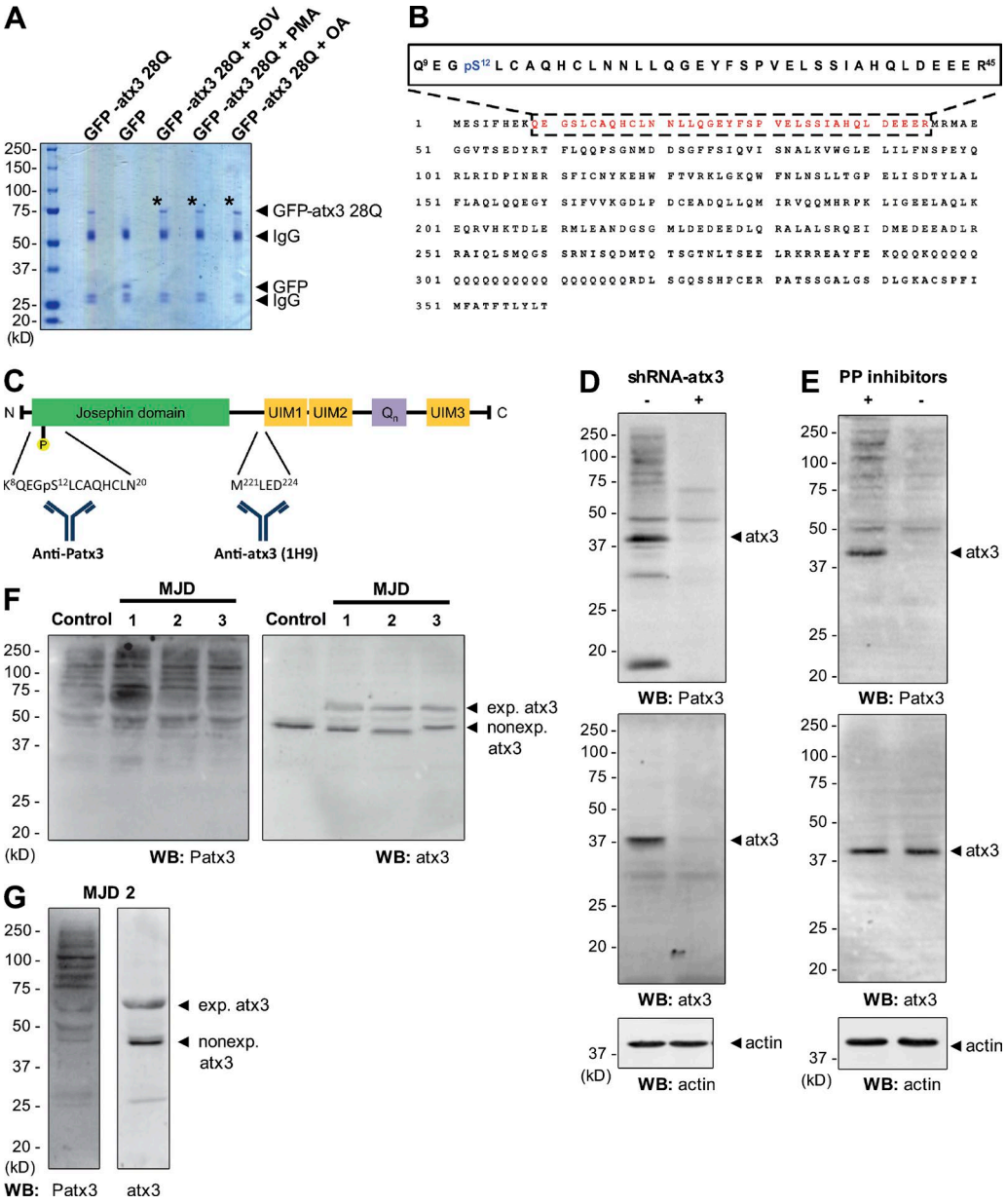

Figure 2. **S12 of atx3 is phosphorylated in neurons.** (A) HEK 293FT cells were transfected with GFP-atx3 28Q and stimulated with phorbol-12-myristate 13-acetate (PMA), sodium orthovanadate (SOV), or okadaic acid (OA) to increase protein phosphorylation levels. GFP-atx3 28Q was immunoprecipitated, separated by SDS-PAGE, and the resulting gel was stained with Coomassie blue, as represented. GFP-atx3 28Q bands (marked with *) were excised and subjected to tryptic digestion and mass spectrometry analysis. (B) Online liquid chromatography followed by ion spray mass spectrometry (LC-ES-MS) detected one phosphorylated peptide in the sample prepared after okadaic acid stimulus and mapped the phosphorylation site to S12. Human atx3 variant MJD1a amino acid sequence (available from GenBank under accession no. AAB33571.1) is shown with the detected phosphopeptide colored in red. (C) A phosphospecific antibody recognizing phosphorylated atx3 S12 was produced. The diagram represents the positions of the S12-containing antigen used during antibody production and the epitope recognized by the anti-atx3 antibody (clone 1H9). (D) Western blot probing of cortical neuron lysates with the anti-Patx3 antibody yielded a protein band corresponding to full-length endogenous atx3 that is absent from cells transduced with atx3-targeting shRNA (sRNA-atx3). Actin was used as a loading control. (E) The endogenous atx3 band displays no immunoreactivity when cell lysates are prepared without phosphatase (PP) inhibitors. (F) Probing of human MJD patient fibroblasts (MJD1–3) and a matched control with the anti-Patx3 antibody reveals a similar protein band pattern to that of neurons. exp., expanded; nonexp., nonexpanded. (G) Increased resolving of patient MJD2 fibroblast sample distinguishes two bands that match the size of expanded (exp.) and nonexpanded (nonexp.) atx3.

previously described (Gales et al., 2005), they were incubated with the substrate Ub-C-terminal 7-amino-4-methylcoumarin (Ub-AMC), and the fluorescence yielded by free AMC was recorded as a measure of product formation. The respective reaction curves reveal that the substrate cleavage rate is higher for 6His-atx3 WT comparing with the phosphomimetic 6His-atx3 S12D (Fig. 4 A). The decreased activity of the phosphomimetic form is expressed by a 43.6 ± 4.7% (SEM) reduction of the initial reaction velocity, when compared with the control (Fig. 4 B).

Incubation of 6His-atx3 WT or 6His-atx3 S12D with K48- and K63-linked chains of six Ub monomers led to the formation of Ub species of lower molecular weight in a time-dependent manner, as assessed by Western blot (Fig. 4, C–F). Consistent with a reduced substrate proteolysis, 6His-atx3

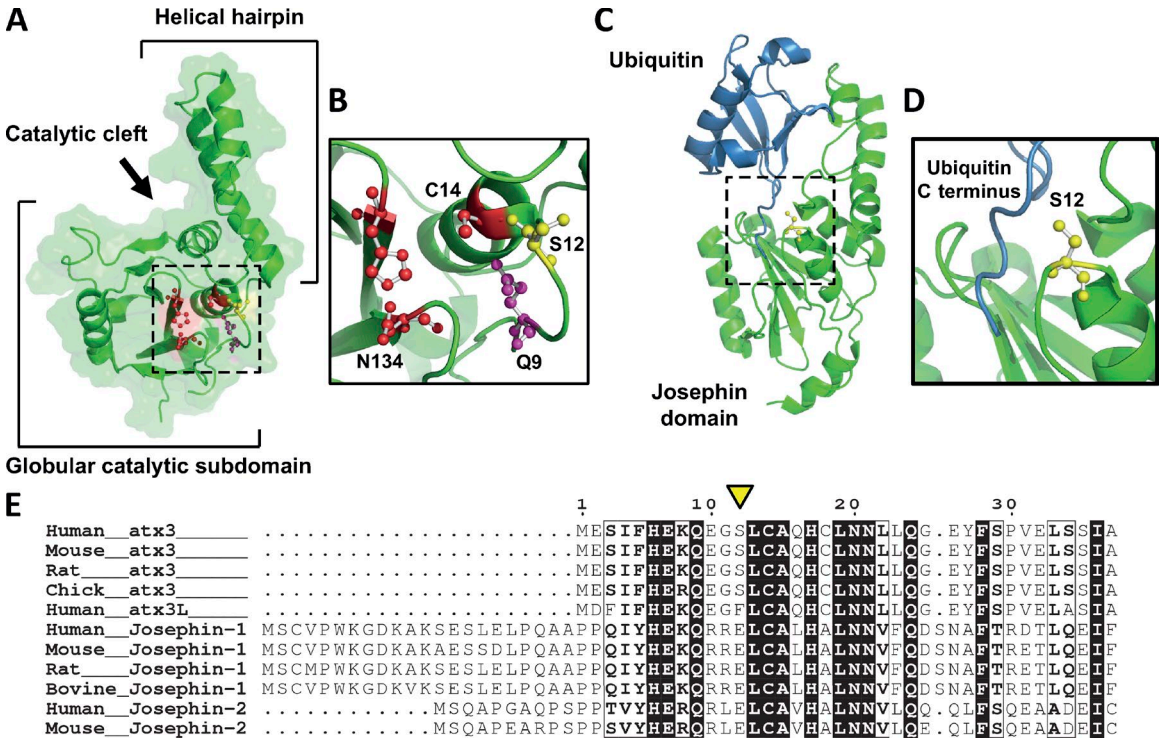

Figure 3. **S12 localizes in the vicinity of atx3 catalytic site.** (A) S12 (yellow) is positioned in the groove between the two subdomains of the JD, (B) in close proximity to the amino acids of the catalytic triad—C14, H119, and N134—and to the residue proposed to form the oxyanion hole—Q9 (PDB ID 1YZB; Nicastro et al., 2005). (C and D) Binding of an Ub molecule to the Ub-binding site 1 of the JD positions the C-terminal region of Ub close to S12 (PDB ID 2JRI; Nicastro et al., 2009). The structures represented in (A–D) were prepared with PyMOL (http://www.pymol.org). (E) S12 (arrowhead) is conserved in vertebrate atx3 but is substituted by a phenylalanine residue in atx3L and by a glutamate residue in Josephin-1 and -2. Protein sequences were obtained from the UniProt database, aligned with the Crustal Omega online tool (http://www.ebi.ac.uk/Tools/msa/clustalo/) and displayed with ESPript 3.0 (Robert and Gouet, 2014). Strictly conserved residues are represented by white letters in a black background and highly similar residues are represented by bold letters in framed columns.

S12D elicited a decreased formation of Ub products comparing with 6His-atx3 WT. This was observed for both types of chains; however, the difference is more prominent in the reaction with the K63-linked chains.

Collectively, these in vitro assays demonstrate that the presence of a negatively charged aspartate at position 12 decreases atx3 DUB activity, suggesting that such is the effect of S12 phosphorylation on atx3 DUB activity.

Mimicking S12 phosphorylation counters morphologic changes caused by expression of pathogenic atx3 in neuronal cultures

We tested whether phosphorylation of S12 interfered with the neuromorphologic defects caused by expanded atx3 expression in cortical neurons. Cultures were transfected with phosphomimetic GFP-atx3 84Q S12D or nonphosphorylatable GFP-atx3 84Q S12A (Figs. 5 A and S2), and total dendritic length was analyzed aspreviously described (see first pragraph of Results). The GFP-atx3 84Q S12A mutant exhibited similar effects to those of GFP-atx3 84Q WT, but neurons expressing GFP-atx3 84Q S12D had higher total dendritic length, showing no differences relative to the total dendritic length of cells expressing GFP-atx3 28Q WT (Fig. 5, A and B). Nonexpanded GFP-atx3 28Q S12A also led to an increased toxicity comparing with the other nonexpanded forms. These results suggest that phosphorylation of S12 protects against dendritic tract loss caused by atx3 polyQ expansion and that compromising this modification is enough to cause a loss of dendritic tracts.

We then investigated whether the S12 phosphomutations affected the number of synaptic contacts in the cultures. Neurons expressing GFP-atx3 84Q S12D show no difference in the number of excitatory glutamatergic synapses (Fig. 6, A and C) and inhibitory postsynaptic terminals (Fig. 6, B and D) compared with GFP-atx3 28Q WT, suggesting that atx3 phosphorylation at S12 rescues the deleterious outcomes of expanded atx3 expression.

The differential effects caused by mutation of S12 hint to the fact that phosphorylation of this amino acid residue counters the morphologic defects caused by expanded atx3 expression in neurons.

Atx3 S12 modulates toxicity induced by pathogenic atx3 in cultured neurons and in vivo

Given the recognized role of aggregation in the toxicity pathways involved in polyQ expansion diseases, we tested whether the S12 phosphomutations affected atx3 tendency to aggregate. It has been demonstrated that atx3 JD is prone to self-assemble in vitro, modulating aggregation of both expanded and nonexpanded atx3 (Masino et al., 2004, 2011; Gales et al., 2005; Ellisdon et al., 2006); changes caused by phosphorylation at S12 could therefore modulate the dynamics of atx3 aggregation.

Cortical neurons were transfected with GFP-tagged WT or phosphomutants S12D or S12A atx3 and scanned in search for GFP-positive accumulations. Cells were counted as having GFP -atx3 aggregation when they presented at least one noticeable instance of GFP-positive accumulation, regardless of size; cells

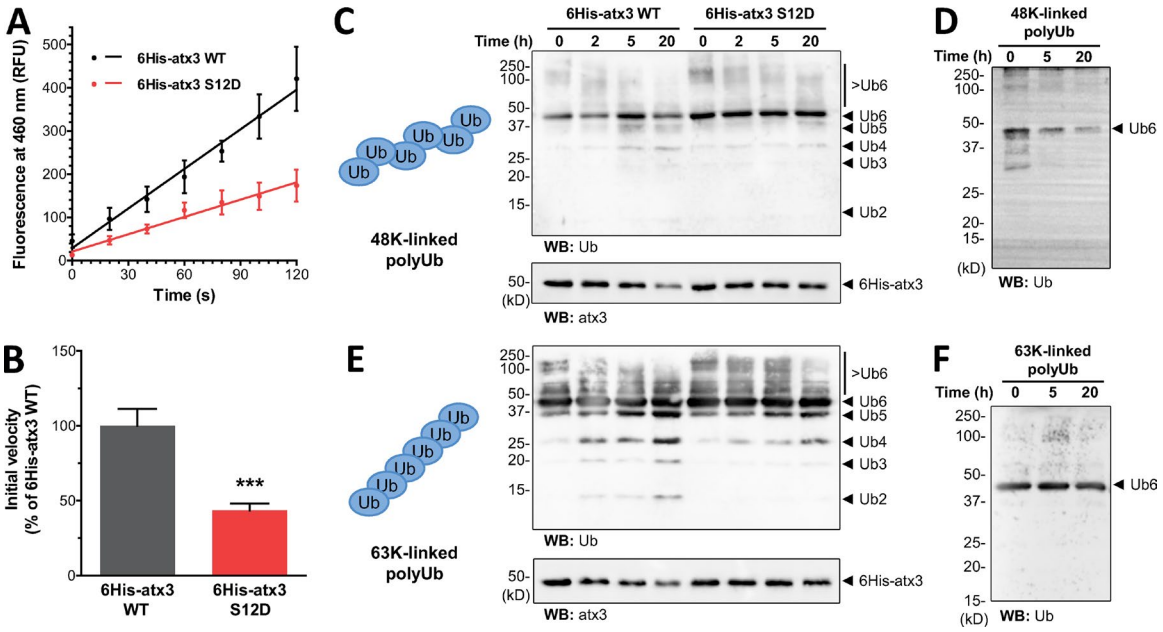

Figure 4. **Mimicking S12 phosphorylation decreases atx3 DUB activity in vitro.** (A) Recombinant 6His-atx3 was incubated with Ub-AMC in vitro, and product formation was assessed by measuring AMC fluorescence. 6His-atx3 S12D shows a decreased Ub-AMC cleavage rate, comparing with 6His-atx3 WT. The panel shows the reaction curve of initial product formation of a representative experiment (n = 3 technical replicates, dots represent mean ± SEM fluorescence values, after subtracting the value of buffer and Ub-AMC only; RFU, relative fluorescence units; two-way ANOVA detected a $P < 0.0001$ significant difference between protein samples). (B) The initial reaction velocity of 6His-atx3 S12D is decreased to 43.6 ± 4.7% in relation to 6His-atx3 WT (n = 8 technical replicates normalized to 6His-atx3 WT, from three independent experiments; graph bars represent mean ± SEM; t test: ***, $P < 0.001$). (C and E) In vitro incubation of 6His-atx3 with K48- or K63-linked hexameric polyUb chains (6Ub) leads to a time-dependent formation of lower molecular weight Ub species (Ub2–5), as assessed by Western blot labeling of Ub species. 6His-atx3 S12D elicits less polyUb cleavage than 6His-atx3 WT. (D and F) PolyUb chains showed no time-dependent degradation in the absence of 6His-atx3.

displaying only diffuse GFP signal were counted as having no aggregates (Fig. 7 A). Expanded GFP-atx3 84Q WT displays a profoundly increased tendency to aggregate compared with GFP-atx3 28Q WT (Fig. 7 B), as expressed by the percentage of cells that presented aggregates in the context of the overall population of transfected cells (GFP-atx3 aggregates in 48.31 ± 10.25% of the cells; n = 5). This is in agreement with the well-known association between the tendency to aggregate and the length of the polyQ sequence, serving as validation to this aggregation assay. Mutation of S12 to aspartate or alanine decreases the fraction of neurons with aggregates, reaching statistical significance in cells transfected with GFP-atx3 84Q S12A (Fig. 7 B). The results suggest that S12 contributes to atx3 aggregation and toxicity in neurons and that modification of this amino acid decreases these effects. The DUB inactive mutant GFP-atx3 84Q C14A (Burnett et al., 2003) exhibits a tendency to aggregate comparable with that of GFP-atx3 84Q WT (Fig. S3), suggesting that the effect of atx3 phosphorylation on atx3 aggregation is not related to its effect on proteolytic activity.

Finally, we explored the changes caused by S12 phosphorylation on the pathogenic events occurring on a lentiviral animal model of MJD with striatal pathology, generated by direct delivery of viral particles encoding full-length human expanded atx3 (72Q) to the striatum of adult animals by stereotaxic injection (Alves et al., 2008b). For each animal, particles encoding atx3 72Q WT were injected into the striatum of the brain's left hemisphere, whereas the striatum of the right hemisphere was injected with particles encoding either atx3 72Q S12D or atx3 72Q S12A (Figs. 8 A and S4). Animals were euthanized 4 wk after injection, and coronal brain slices of the whole striatal region were immunohistochemically processed and analyzed.

Slices were labeled with an anti-atx3 antibody, and the regions of the striatum demonstrating atx3 aggregation were imaged and the number of inclusions was quantified (Alves et al., 2008a; Nascimento-Ferreira et al., 2011). Transduction of the rat striatum with atx3 72Q led to the formation of detectable aggregates (Fig. 8, B and C), in agreement with what has been described for this animal model. Mutation of S12 to aspartate or alanine significantly decreased the amount of inclusions formed, comparing with atx3 72Q WT (Fig. 8, F and G).

Examination of the severity of neurodegeneration caused by each atx3 72Q form was performed by labeling the slices with an antibody detecting a neuronal marker: dopamine- and cyclic AMP-regulated phosphoprotein of 32 kD (DARPP-32). Expression of atx3 72Q led to a localized loss of anti–DARPP-32 antibody immunoreactivity, compatible with the toxicity expected of atx3 with a pathogenic polyQ expansion (Fig. 8, D and E). Nonetheless, the volume of the DARPP-32–depleted region was reduced in the case of the injections with the phosphomutants, comparing with atx3 72Q WT (Fig. 8, H and I).

Excitatory synapses were labeled in striatal slices with antibodies detecting the postsynaptic protein PSD-95 and the presynaptic vesicular transporter VGLUT1, and the immunoreactivity signal of each marker was imaged in the vicinity of atx3 72Q–expressing neurons (Fig. 8, J, L, N, and P). The integrated density of PSD-95 and VGLUT1 agglomerates was quantified through a range of detection thresholds and found to be increased in the striatal slices expressing phosphomutated (S12A or S12D) atx3 72Q, comparing with slices expressing atx3 72Q WT (Fig. 8, K, M, O, and Q), suggesting that phosphorylation of S12 decreases excitatory synapse loss associated with the expression of expanded atx3 in the rat striatum.

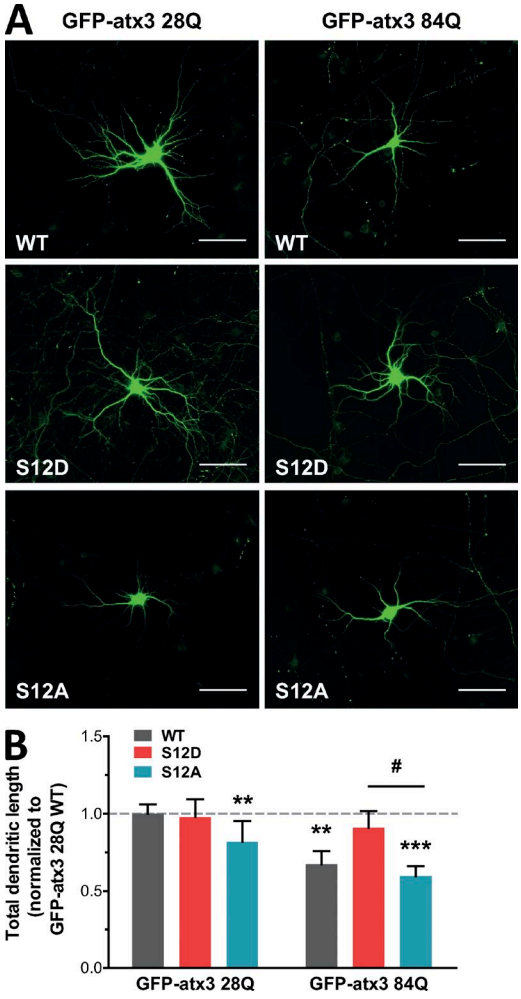

Figure 5. **Mimicking S12 phosphorylation reduces dendritic tract loss caused by expression of expanded atx3 in cortical neurons.** (A) Rat cortical neuron cultures were transfected with phosphomutants S12D and S12A of GFP-atx3 28Q and GFP-atx3 84Q. Panels show representative fluorescence microscopy images of the cell body and dendritic trees of transfected neurons. Bars, 100 µm. (B) Expression of phospho-null GFP-atx3 84Q S12A causes a reduction of total dendritic length, but transfection with GFP-atx3 84Q S12D elicits no differences, comparing with the GFP -atx3 28Q WT control (n = 16–21 neurons, from two independent experiments; graph bars represent mean ± SEM; comparison with GFP-atx3 28Q WT was performed with the Mann-Whitney t test: **, $P < 0.01$; ***, $P < 0.001$; two-way analysis of variance followed by Bonferroni post hoc test compared between other pairs of conditions: #, $P < 0.05$).

The observations made in the MJD lentiviral rat model indicate that phosphomutation of S12 decreases expanded atx3 aggregates and cytotoxicity, in vivo.

Discussion

Approaches to MJD treatment may benefit from a deepened comprehension of the reversible pathways that interfere with the cellular defects caused by pathogenically expanded atx3. This study demonstrates that polyQ expansion of the protein causes a loss of dendrites and synapses that is countered by simulating phosphorylation of the protein at S12. Importantly, mutation of this novel phosphorylation site reduces the tendency of pathogenic atx3 to aggregate and induce neuronal demise in vivo, suggesting that phosphorylation of S12 of atx3 may have a protective effect in the context of MJD (Fig. 9).

The phosphospecific anti-Patx3 antibody that was generated detected phosphorylated atx3 in cortical neurons and human fibroblasts for the first time, indicating that phosphorylation of S12 is physiologically relevant. We investigated neuron-specific changes in cellular morphology in cortical cultures, considering the growing evidence implicating the cerebral cortex in the pathogenic mechanisms (Yamada et al., 2001; Alves et al., 2008b; Pedroso et al., 2013; Rüb et al., 2013): authors have described reduced glucose metabolism (Soong et al., 1997; Taniwaki et al., 1997) and atrophy in the cortex of MJD patients' brain (Murata et al., 1998; D'Abreu et al., 2012; Lopes et al., 2013) and the presence of polyQ inclusions (Yamada et al., 2001; Ishikawa et al., 2002). Although cortical neurons are not frequently found to visibly degenerate, it is possible that they are dysfunctional in MJD; the presence of inclusions may reflect this dysfunction, even if it is not causatively involved (Schöls et al., 2004). In our experiments, the presence of an expanded polyQ sequence in transfected GFP-atx3 led to a morphologic phenotype, with contracted dendrites, fewer excitatory synapses, and a decreased number of inhibitory postsynaptic terminals. Previous studies using neurons from transgenic *Drosophila* larvae have detected dendritic abnormalities resulting from expanded atx3 expression (Lee et al., 2011), and a severe impairment of dendritic arborization was also recently described to occur in the Purkinje cells of a MJD mouse model (Konno et al., 2014). Our results constitute the first evidence that full-length expanded atx3 causes an observable dendritic loss/shrinkage and synapse loss in mammalian neuron cultures, suggesting that similar events may take place in MJD patient brains. The changes we observe may also occur in brain regions other than the cortex, representing a wider neuronal-specific mechanism of cellular dysfunction. The possibility of a disruption of neuronal structure—and, consequently, function—without or before cell death triggering supports the prevalent idea of an involvement of synaptic dysfunction in the pathogenesis of MJD (Chou et al., 2008; Boy et al., 2010; Shakkottai et al., 2011).

Mutation of S12 to negatively charged aspartate reduced the dendritic demise and synaptic loss caused by polyQ-expanded atx3 expression in cortical neurons; contrastingly, the effects of the phospho-null mutant were similar to those of the nonmutated expanded atx3. These results suggest that phosphorylation at S12 may be able to counter the cellular defects caused by atx3 expansion. Additionally, the fact that these defects are reversible on mutation of a single residue, which is distant from the polyQ stretch, suggests that atx3 may be functionally involved in the development or maintenance of dendrites and synapse in vivo. Our results suggest that S12 phosphorylation contributes to this function, which would be disrupted on polyQ expansion. Thus far, atx3 has never been demonstrated to play any clear function which would be critical for neuronal survival and activity, but it was recently reported to be involved in neuronal differentiation of neuroblastoma cells (Neves-Carvalho et al., 2015). Atx3 involvement with dendrite and synapse maintenance may be mediated through its reported participation in cell pathways, including transcriptional regulation (Rodrigues et al., 2007; Chou et al., 2008), protein quality control, and cytoskeletal organization (Rodrigues et al., 2010). Future studies will be needed to determine if dendrite retraction and synaptic loss on atx3 expansion result from the disturbance of any of these functions.

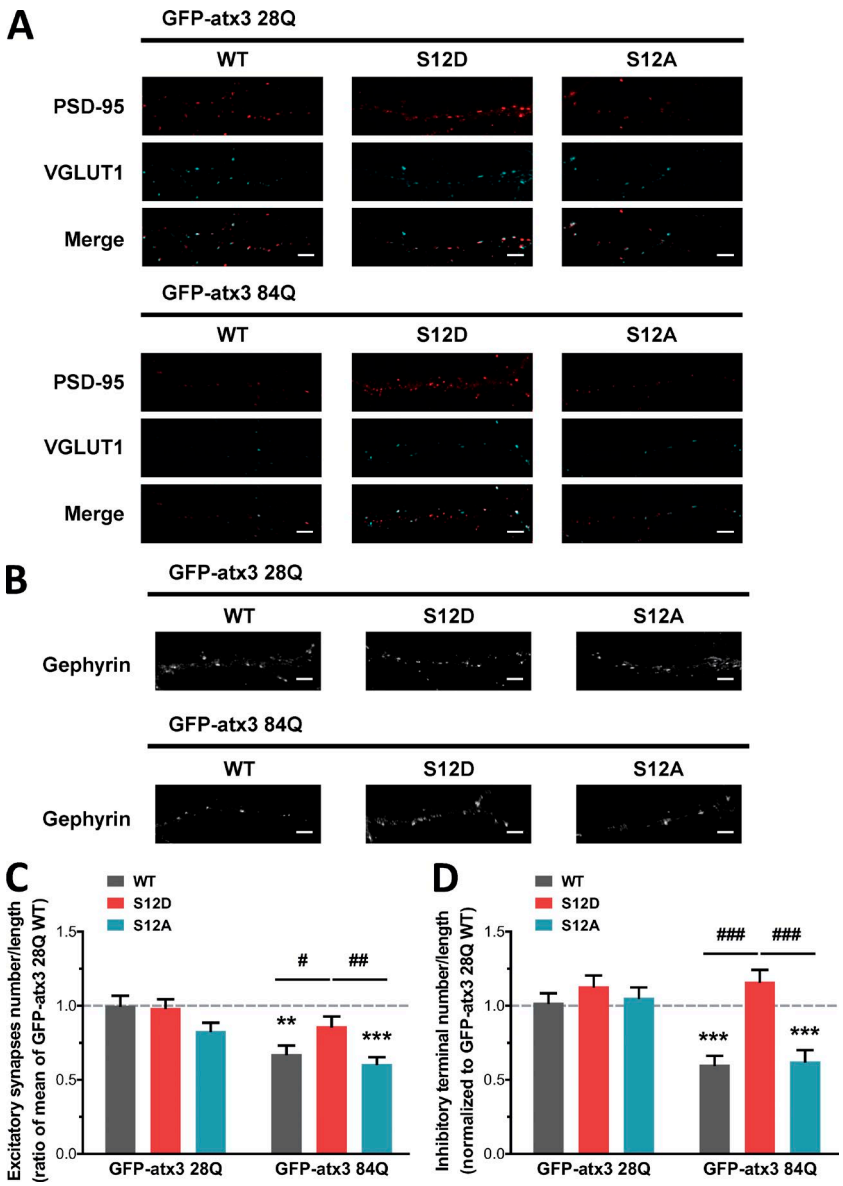

Figure 6. **Mimicking S12 phosphorylation reduces synapse loss elicited by expanded atx3 expression in cortical neurons.** (A and B) Rat cortical neuron cultures were transfected with phosphomutants S12D and S12A of GFP-atx3 28Q and GFP-atx3 84Q. The panels show representative fluorescence microscopy sections from dendritic tracts of GFP-atx3–expressing neurons, evidencing (A) glutamatergic synapse markers VGLUT1 and PSD-95–positive puncta and the respective colocalization (merge) or (B) gephyrin-positive puncta. Bars, 5 µm. (C) Expression of the GFP-atx3 84Q S12A mutant causes a decrease in the number of functional glutamatergic synapses, comparing with the expression of GFP-atx3 28Q WT. Phosphomimetic GFP-atx3 84Q S12D causes no significant reduction (n = 24–32 neurons, from three independent experiments; graph bars represent mean ± SEM; comparison with GFP-atx3 28Q WT was performed with the Mann-Whitney t test: **, $P < 0.01$; ***, $P < 0.01$; two-way analysis of variance followed by Bonferroni post hoc test compared between other pairs of conditions: #, $P < 0.05$; ##, $P < 0.01$). (D) GFP-atx3 84Q S12D expression does not produce the loss of inhibitory postsynaptic terminals caused by GFP-atx3 84Q WT and S12A, as inferred from the number of gephyrin-containing puncta (n = 24–30 neurons, from three independent experiments; graph bars represent mean ± SEM; comparison with GFP-atx3 28Q WT was performed with the Mann-Whitney t test: ***, $P < 0.001$; two-way analysis of variance followed by Bonferroni post hoc test compared between other pairs of conditions: ###, $P < 0.001$).

The in vitro assays show that S12 phosphorylation regulates atx3 DUB activity, adding to the previously described effect of ubiquitination of K117 at the JD, which enhances the DUB activity of the protein (Todi et al., 2010). In the cell environment, conjugation of a phosphate group to S12, localized in the catalytic domain of atx3, might affect the neighboring amino acid residues, as a consequence of steric constraints and/or imposed by the negative charge of the phosphate group. Changes in the amino acids comprising the catalytic triad or alterations that could affect substrate binding and/or positioning, such as in the conformation of the closely positioned Ub-binding site 1 of the JD helical hairpin, might result in changes of proteolytic activity (Nicastro et al., 2005, 2009; Hunter, 2007; Tarrant and Cole, 2009; Huang et al., 2012; Renatus and Farady, 2012). Notably, the crystal structure of the complex formed by Ub and the ataxin-3–like protein (atx3L) JD revealed that the phenylalanine at position 12 forms a hydrophobic enclosure with other aromatic amino acid around the active center, through which the C terminus of the Ub molecule threads (Weeks et al., 2011). The position appears to be suitable for interaction with the lysine side chain forming the isopeptide bond. It has been reported that mutation of S12 of the atx3 JD to a phenylalanine increases proteolysis of Ub substrates (Weeks et al., 2011), consistent with the relevance of this residue in determining atx3 activity that our results propose. Phosphorylation of S12 may therefore modulate important aspects of atx3 biologic activity, such as the cleavage rate of particular atx3 substrates and/or the molecular interactions established by the protein. The consequences of these changes may have different cellular outcomes, possibly related to the maintenance of specialized neuronal structures.

S12 is highly conserved in atx3 vertebrate homologues, but is substituted by different residues in other JD-containing proteins: a negatively charged glutamate in Josephin-1 and -2 and an aromatic phenylalanine in atx3L (Fig. 3 E). In agreement with our results showing that S12 phosphorylation decreases the proteolytic activity of atx3, the activity of the JDs isolated from human atx3, atx3L, Josephin-1, and Josephin-2 has been shown to be markedly different when tested against several different Ub model substrates in vitro (Weeks et al., 2011). Although the variations reported may be attributed to other sequence or structural differences between the protein JDs, it is possible that the residue occupying the position of S12 plays a role in modulating enzyme activity.

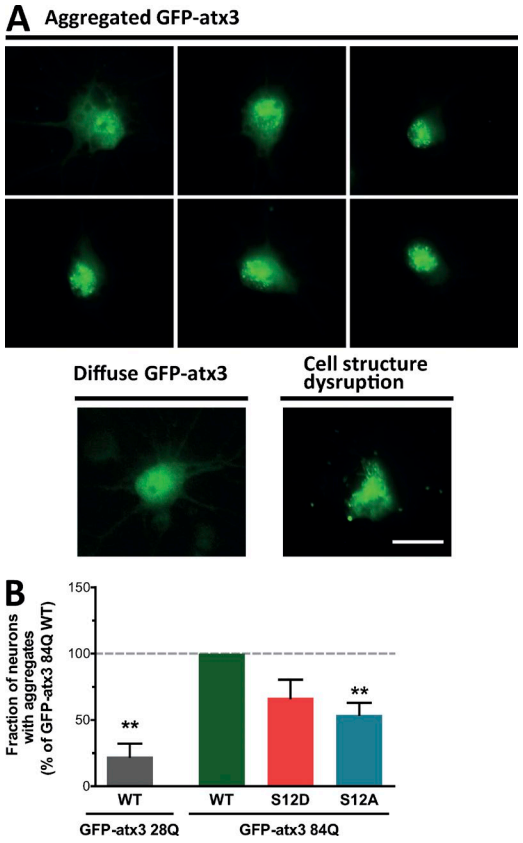

Figure 7. **Mutating S12 decreases expanded atx3 aggregation in cortical neurons.** (A) GFP-atx3 accumulates in the cell body of a fraction of transfected cortical cultures. The number of cells with GFP-atx3 aggregates was counted versus the number of cells presenting only diffuse GFP -atx3 signal; neurons displaying a compromised structure were excluded from the counting. The panels illustrate the diversity of the aggregates obtained. Bar, 20 µm. (B) Mutating S12 of GFP-atx3 84Q decreases the fraction of cells with aggregates comparing with what is caused by GFP -atx3 84Q WT. The decrease reaches statistical significance with GFP-atx3 84Q S12A (17–59 neurons were counted for each condition in $n = 5$ independently prepared cultures; graph bars represent mean ± SEM; one-sample t test: **, $P < 0.01$).

Mutation at serine 12 to aspartate or alanine reduces the tendency of expanded GFP-atx3 to form aggregates in cultures neurons. It has been hypothesized that atx3 aggregation is dependent on the molecular interactions it establishes, and in vitro association of the JD with Ub protects against aggregation (Song et al., 2010; Masino et al., 2011). The two Ub-binding sites in the catalytic JD overlap with the regions described as taking part in JD self-assembly (Nicastro et al., 2009; Masino et al., 2011), and interestingly, S12 is in close proximity to the Ub-binding site 1. Taking all this into consideration, mutation at S12 may reduce aggregation by interfering with the interactions modulated by Ub-binding site 1, possibly favoring interactions that protect against atx3 aggregation. The fact that the inactive C14A mutant leads to an aggregation profile similar to that of GFP-atx3 84Q supports the idea that this effect on aggregation is not related to the decrease in DUB activity caused by phosphorylation. Furthermore, phosphomutation of S12 does not alter atx3 subcellular localization (in COS-7 cells; Fig. S5, A–D), indicating that the decrease on aggregation may not involve a decreased nuclear distribution of the protein.

When the phosphomutants of atx3 are expressed in the striatum of injected rats, they lead to a decreased inclusion formation and neurodegeneration comparing with the nonmutated protein, suggesting that S12 modification has a protective effect in vivo. This similar effect of the phosphomimetic and the phospho-null mutations is not unique. In a study describing the effects of huntingtin phosphorylation at T3, although each phosphomutant of T3 had opposed tendencies to aggregate, both mutations were neuroprotective in a *Drosophila* model, reducing lethality and neurodegeneration (Aiken et al., 2009). Our results indicate that the availability of S12 is an important factor contributing to toxicity-related events in neurons. We suggest that nonphosphorylated S12 of expanded atx3 may contribute to pathways turning the protein more toxic, precipitating events such as misfolding, cleavage, or aggregation. Consequently, modifications targeting S12 may reduce the toxicity of expanded atx3, with possible protective outcomes. In a biologic context, the modifications caused by phosphorylation of S12 are likely to influence pathogenic mechanisms mediated by this amino acid. Phosphorylation of S12, as a biologic device that actually turns it into a different chemical entity, could have an effect of "turning off" the toxic mechanisms in which S12 takes part.

The ameliorating effects of the phosphomimetic mutations in our cell culture and in vivo models of MJD strongly suggest that S12 phosphorylation is protective against the toxicity of expanded atx3. Further studies will inform on the usability of the modulation of S12 phosphorylation state as a target for MJD therapy.

Materials and methods

Expression plasmids and lentiviral vectors

Eukaryotic expression pEGFP-C1 plasmids encoding human atx3 variant MJD1a (available from GenBank under accession no. AAB33571.1) with 28 glutamines (GFP-atx3 28Q) or 84 glutamines (GFP-atx3 28Q) N terminally fused with GFP (Chai et al., 1999) and pFLAG-CMV-6a plasmids encoding human atx3 variant MJD1-1 (available from GenBank under accession no. NP_004984.2) with 22 glutamines (FLAG-atx3 22Q) or 80 glutamines (FLAG-atx3 80Q) N terminally fused with FLAG were a gift from H. Paulson (University of Michigan, Ann Arbor, MI). Empty vector pEGFP-C1 was obtained from BD Biosciences (available from GenBank under accession no. U55763). Eukaryotic expression plasmid SIN-W-PGK encoding human atx3 variant MJD1a with 72 glutamines and an N-terminal Myc tag (atx3 72Q) and plasmid SIN-CW-PGK-nls-LacZ-LTR-TRE encoding an universal short hairpin targeting human and rat atx3 (shRNA-atx3) were previously produced by our group (Alves et al., 2008b, 2010). Constructs used in the viral production (pCMVDR-8.92, pMD.G, and pRSV-Rev) have been described previously (de Almeida et al., 2002) and were a gift from N. Deglon (University Hospital of Lausanne, Lausanne, Switzerland). Bacterial expression pDEST17 plasmid encoding N-terminally 6His-tagged human atx3 isoform MJD1-1 with 13 glutamines (6His-atx3) was previously generated by our group (Gales et al., 2005).

Site-directed mutagenesis of the expression constructs was performed using the QuickChange Site-Directed Mutagenesis kit (Stratagene) or the QuikChange II XL Site-Directed Mutagenesis kit (Agilent Technologies). Phosphomimetic S12D mutants, with aspartate at position 12, were generated using primers (forward) 5′-CACGAG AAACAAGAAGGCGACCTTTGTGCTCAACATTGCCTG-3′ and (reverse) 5′-CAGGCAATGTTGAGCACAAAGGTCGCCTTCTTG TTTCTCGTG-3′. Phospho-null S12A mutants, with alanine at posi-

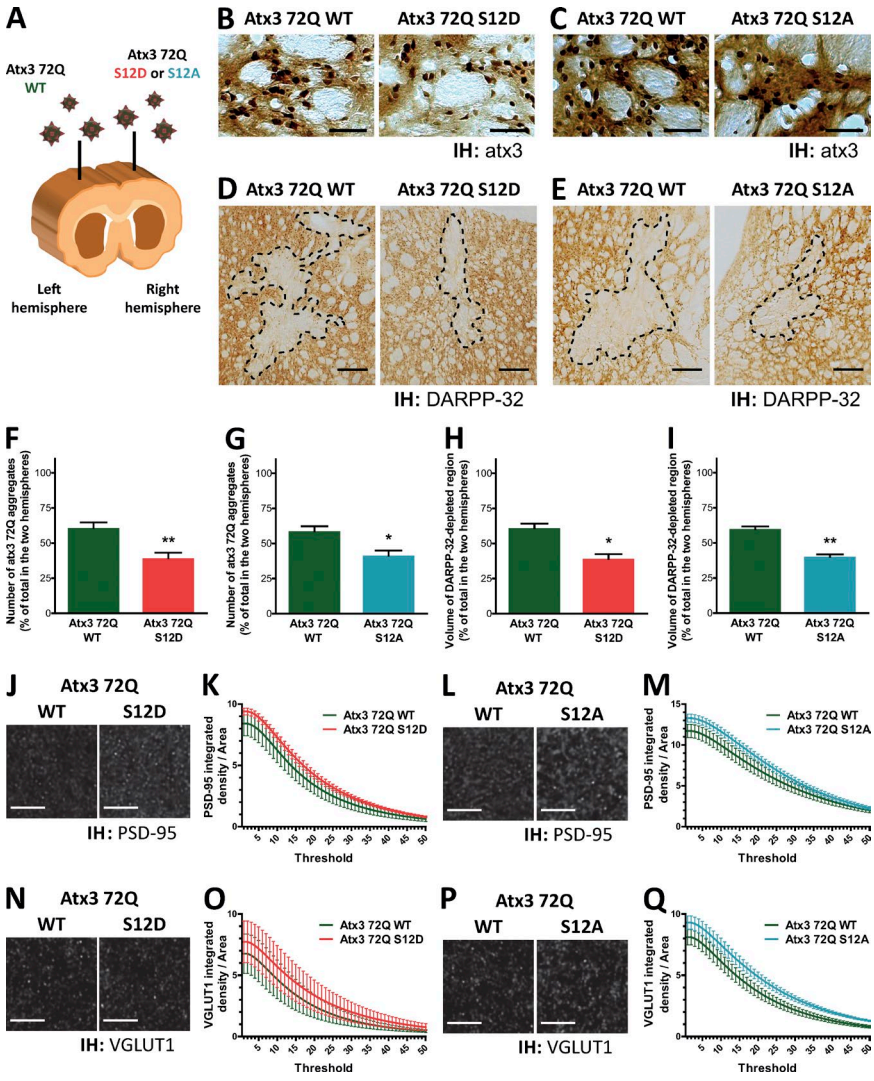

Figure 8. **Mutating S12 reduces the neurodegenerative phenotype of a MJD lentiviral rat model.** (A) Atx3 72Q–encoding lentiviral particles were stereotaxically delivered into rat striata: the left hemisphere striatum was injected with atx3 72Q WT and the right hemisphere with one of its phosphomutants—S12D or S12A. (B and C) Atx3 was immunohistochemically (IH) labeled and atx3 accumulations were quantified. Representative images of the peroxidase staining of striatal sections displaying atx3-positive aggregates are shown. Bars, 50 µm. (F and G) Mutating S12 reduces the amount of atx3 accumulations caused by atx3 72Q expression ($n = 7$ animals injected with atx3 72Q WT: atx3 72Q S12D; $n = 6$ animals injected with atx3 72Q WT: atx3 72Q S12A; graph bars represent mean ± SEM; Mann-Whitney test: *, $P < 0.05$; **, $P < 0.01$). (D and E) Neuronal loss was assessed by determining the volume of the DARPP-32 immunoreactivity-depleted region in each hemisphere. Representative images of the peroxidase staining of striatal sections evidencing immunoreactivity loss (interrupted line) are shown. Bars, 300 µm. (H and I) Mutating S12 of atx3 reduces the lesion caused by atx3 72Q injection into the rat striatum, as evaluated by DARPP-32 immunostaining ($n = 4$ animals injected with atx3 72Q WT: atx3 72Q S12D; $n = 5$ animals injected with atx3 72Q WT: atx3 72Q S12A; graph bars represent mean ± SEM; Mann-Whitney test: *, $P < 0.05$; **, $P < 0.01$). (J, L, N, and P) Excitatory synapse markers PSD-95 and VGLUT1 were immunohistochemically labeled and imaged in the vicinity of atx3 72Q–expressing neurons. Panels show representative confocal images of PSD-95 (J and L) and VGLUT1 (N and P) punctuate immunostaining. Bars, 5 µm. (K, M, O, and Q) The integrated density of PSD-95 and VGLUT1 agglomerates is increased in the striatal slices expressing phosphomutated atx3 72Q, comparing with slices expressing atx3 72Q WT, throughout the range of detection thresholds used ($n = 3$ animals for each injection condition; graph bars represent mean ± SEM; two-way analysis of variance detected a $P < 0.001$ significant difference between hemispheres).

tion 12, were obtained with primers (forward) 5′-CACGAGAAACAAGAAGGCGCACTTTGTGCTCAACATTGCCTG-3′ (reverse) 5′-CAGGCAATGTTGAGCACAAAGTGCGCCTTCTTGTTTCTCGTG-3′. DUB activity-deficient C14A mutants, with alanine at position 14, were produced with primers (forward) 5′-GAGAAACAAGAAGGCTCACTTGCTGCTCAACATTGCCTG-3′ and (reverse) 5′-CAGGCAATGTTGAGCAGCAAGTGAGCCTTCTTGTTTCTC-3′. Mutation was confirmed after automatic DNA sequencing (STAB VIDA).

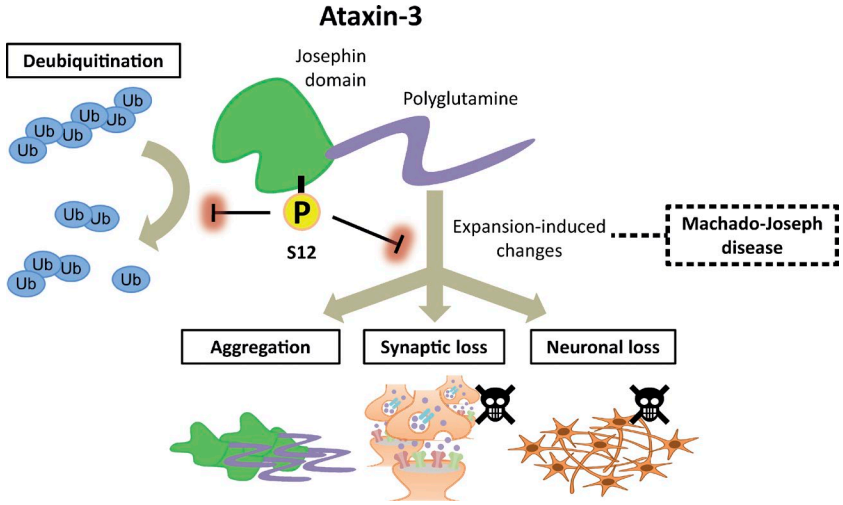

Figure 9. **Phosphorylation of atx3 at S12 counters toxic polyQ expansion–derived changes.** Atx3 is phosphorylated at S12, an amino acid localized in the catalytic JD of the protein. Current results suggest that this modification decreases the hydrolytic activity of atx3 against polyUb chains. S12 phosphorylation in atx3 reduces expanded atx3 aggregation, decreases dendritic and synaptic loss caused by the expanded protein in neurons, and limits neurodegeneration.

Cell line culture and transfection

HEK 293FT cells were grown in DMEM, pH 7.2, supplemented with 44 mM $NaHCO_3$, 10% FBS, 0.1 mM nonessential amino acids, 6 mM L-glutamine, 1 mM sodium pyruvate, and 500 µg/ml geneticin. COS -7 cells were cultured in DMEM, pH 7.2, supplemented with 44 mM $NaCO_3$, 10% FBS, and 1% penicillin-streptomycin. Both cell lines were maintained at 37°C, in a humidified atmosphere containing 5% CO_2.

One day before transfection, fully confluent cells were diluted (1:6) and seeded onto 100-mm culture plates, and transient transfection was performed after 24 h of cell growth, using the Lipofectamine Transfection Reagent for HEK293FT cells (Life Technologies) or the Lipofectamine LTX Transfection Reagent (Life Technologies) for COS-7 cells. Expression was left to occur for 24–48 h before extracts were prepared.

Viral production

Lentiviral vectors encoding atx3 72Q or shRNA-atx3 were produced in HEK 293T cells using the four-plasmid system described previously (de Almeida et al., 2002). In brief, HEK 293T cells (cultured as described for COS-7 cells) were plated into 100-mm dishes (4×10^6 cells/dish) and subjected the following day to transient calcium phosphate transfection. DNA complexes were formed by mixing 0.5 M $CaCl_2$ with the DNA constructs (for each plate: 13 µg of the pCMVDR-8.92 packaging construct, 3.75 µg of pMD2G, 3 µg of pRSV-Rev, and 13 g of SIN-W-PGK-ATX3 72Q WT, S12D or S12A, or shAtaxUNIV), to a final concentration of 0.25 M $CaCl_2$. The solution was stirringly mixed with an equal volume of Hepes-buffered solution (280 mM NaCl, 1.5 mM Na_2HPO_4, and 100 mM Hepes, pH 7.1), and 1 ml of DNA complexes was added to each dish. Cells were incubated at 37°C, in a humidified atmosphere containing 3% CO_2, for 6 h, after which transfection media was replaced with fresh culture medium. After 48 h of culture incubation at 37°C, 5% CO_2, the supernatants were collected, filtered (0.45 µm Stericup Filter Unit; Merck Millipore), concentrated by ultracentrifugation (90 m, 19.000 *g*, 4°C), and resuspended in PBS with 1% BSA. When the viral particles were aimed at animal striatal injections, this was followed by another ultracentrifugation step before final resuspension in the same solution. The content level of batches was assessed by p24 antigen ELISA (Retrotek HIV-1 p24 Antigen ELI SA; Zepto Metrix), and stocks were stored at –80°C.

Immunoprecipitation and mass spectrometry analysis

HEK 293FT cells were stimulated with 20 nM okadaic acid for 16 h, 5 mM sodium orthovanadate for 30 min, or 200 nM PMA for 20 min. Cells were scraped unto immunoprecipitation buffer (20 mM Tris, pH 7.0, 100 mM NaCl, 2 mM EDTA, 2 mM EGTA, 50 mM NaF, and 1 mM Na_3VO_4), supplemented with 1% Triton X-100, 1 µM okadaic acid, and protease inhibitors (1 mM DTT, 0.1 mM PMSF, 10 µg/ml chymostatin, pepstatin, antipain, and leupeptin [CLAP]), sonicated, and cleared of the insoluble fraction by centrifugation. 1 mg of protein from each extract (1 mg/ml) was used for immunoprecipitation with 3 µg of anti-GFP antibody (clones 7.1 and 13.1; Roche Applied Science). Protein samples were eluted with 50 µl SDS-PAGE 2× loading buffer (125 mM Tris, pH 6.8, 100 mM glycine, 40% glycerol, 4% SDS, 200 mM DTT , and ∼0.01% bromophenol blue). Three samples of each extract were subjected to the i.p. procedure, but collectively eluted in sequence.

Immunoprecipitants (100 µl) were alkylated (1% acrylamide, 20 min) and separated by SDS-PAGE. Online liquid chromatography followed by ion spray mass spectrometry analysis of the protein bands was performed by the Proteomics Center at the Children's Hospital Boston. Samples were digested in-gel with 12.5 ng/µl trypsin, overnight, at 37°C, and resulting peptides were extracted with 100 mM ammonium bicarbonate and acetonitrile and lyophilized. Samples were resuspended in 5% acetonitrile, 5% formic acid, and directly injected into a liquid chromatography–mass spectrometry system encompassing a microautosampler, a Suvery high performance liquid chromatography pump, and a Proteome X (LTQ) mass spectrometer (all acquired from Thermo Finnigan). Peptides were eluted with 0.1% formic acid in acetronitrile (30 min linear gradient 8–34% acetonitrile) and applied to the mass spectrometer by electrospray ionization. The mass spectrometric data obtained were searched against the human international protein index database (IPI human 336) using the protein identification software Mascot (version 2.2.04; Matrix Sciences), according to the appropriate search criteria necessary for the detection of phosphorylation.

Generation of the anti-Patx3 phosphospecific antibody

Production of the phosphospecific anti-Patx3 antibody was performed by Eurogentec. Rabbits were immunized with a phosphorylated atx3-based peptide—8KQEG-S(PO_3H_2)-LCAQHCLN20—coupled with the keyhole limpet hemocyanin protein carrier. Phosphospecific antibody purification was performed on the serum of the best responding animal (as evaluated by ELISA) through affinity chromatography procedures.

Cortical neuron cultures preparation and transfection

Cortices of Wistar rat embryos with 18 d were dissected, trypsinized, and resuspended in neuronal plating medium (MEM supplemented with 10% horse serum, 0.6% glucose, and 1 mM sodium pyruvate). Cells were passed through a 0.2-µm filter and then seeded in high, medium, or low density, according to the experimental objectives: high-density cultures: 9×10^5 cells/well in six-well culture plates coated with poly-D-lysine (0.1 mg/ml); medium-density cultures: 2.5×10^5 cells/well onto coated 15-mm coverslip-containing 12-well culture plates; and low-density cultures (Banker cultures): 3.25×10^5 cells/plate in 60-mm culture plates containing coated 18-mm coverslips. For high- and medium-density cultures, 2–4 h later, platting medium was substituted by Neurobasal medium supplemented with 2% SM1, 0.5 mM glutamine, and 0.12 mg/ml gentamycin. In the Banker cultures, after 2–3 h, coverslips were turned over an astroglial feeder layer (grown in MEM supplemented with 10% horse serum, 0.6% glucose, and 1% penicillin-streptomycin) and maintained in supplemented Neurobasal medium. Neuronal cultures were kept in an incubator at 37°C, with a humidified atmosphere containing 5% CO_2, up to 15 days in vitro (DIV). High- and medium-density cultures were fed once a week, and low-density cultures were fed twice a week, by replacing 1/3 of the culture medium with fresh medium.

Expression plasmids were transfected by a calcium phosphate transfection procedure adapted from a previously described protocol (Jiang et al., 2004). In brief, DNA complexes were generated by adding 2.5 M $CaCl_2$ in 10 mM Hepes drop-wise to the plasmid DNA solutions, for a final concentration of 250 mM $CaCl_2$. High-density cultures were transfected at 9–10 DIV cortical neurons using 10 µg of plasmid DNA; medium-density cultures were transfected at 4–5 DIV with 4 µg plasmid DNA; and low-density cultures were transfected at DIV 9–10 with 3 µg DNA. Complexes were mixed with an equal volume of Hepes-buffered transfection solution (274 mM NaCl, 10 mM KCl, 1.4 mM Na_2HPO_4, 11 mM dextrose, and 42 mM Hepes, pH 7.2) and added to the cultures. Cells were incubated for 1–1.5 h, after which transfection medium was substituted by fresh culture medium. Kynurenic acid (2 mM) was used throughout the transfection procedure to block ionotropic glutamate receptors. Expression was left to occur for a maximum of 5 DIV under normal cell culture incubation conditions.

Atx3 knock-down and neuronal lysate preparation

High-density rat cortical cultures (8 DIV) were transduced with shRNA -atx3–encoding lentiviral particles (20 ng of p24 antigen/10^5 cells) in the presence of 8 µg/ml hexadimethrine bromide. 18 h later, the

infection medium was substituted by a mixture of conditioned medium and fresh medium (1:2), and expression was left to occur for 6 d under normal culture conditions.

Human fibroblast culture

Human fibroblast cells from MJD patients and a matched control were obtained from Neurology and Pathology Services, University Hospital of Coimbra. Cultures were maintained under 37°C, 5% CO_2 incubation, in DMEM, pH 7.2, supplemented with 44 mM $NaHCO_3$, 10% FBS, 0.1 mM nonessential amino acids, 2 mM L-glutamine, 1 mM sodium pyruvate, and 1% penicillin-streptomycin.

Cell lysate preparation

Lysates were prepared by scraping cultures onto RIPA buffer (10 mM Tris-HCl, pH 7.2, 150 mM NaCl, 5 mM EDTA, 0.1% Triton X-100, 1% sodium deoxycholate, and 0.1% SDS), supplemented with protease (1 mM DTT, 0.1 mM PMSF, and 10 µg/ml CLAP) and phosphatase inhibitors (5 mM NaF, 2 mM Na_3VO_4, and 1 µM okadaic acid), sonicated, and freeze-thawed. After, protein quantification samples were denatured by adding 5× loading buffer (625 mM Tris-HCl, pH 6.8, 50% glycerol, 10% SDS, 500 mM DTT, and ∼0.01% bromophenol blue) and heating to 95°C.

In vitro activity assays

6His-atx3 produced in BL21(DE3)-SI cells was purified as described previously by our group (Gales et al., 2005). Incubation of protein samples (200 µM) with 0.5 µM Ub-AMC (Boston Biochem) was performed in the presence of 20 mM Hepes, pH 7.5, 5% glycerol, and 1 mM EDTA, 0.1 mg/ml BSA, and 10 mM DTT, in 96 well plates. Product formation was assessed at 30°C by fluorescence recording (excitation: 380 nm; emission: 460 nm). For each technical replicate, initial reaction velocity was calculated as the slope of the trend line traced based on the fluorescence values (relative fluorescence units) of the first 2 min of reaction, after subtraction of the value of the negative control lacking 6His-atx3 (with an additional 0.2 M BSA). The obtained velocity values were normalized to the mean WT velocity of the respective experiment.

Incubation of the samples (100 nM) with 250 nM K48- or K63-linked hexameric polyUb chains (Boston Biochem) was performed after mixing with 50 mM Hepes, 0.5 mM EDTA, 0.1 µg/ml ovalbumin, and 1 mM DTT and left to occur for 20 h, at 37°C. Samples (10 µl) were taken from the reaction mixture at 0, 2, 5, and 20 h and immediately denatured by adding 2× concentrated sample buffer.

SDS-PAGE and Western blot

Equivalent protein amounts of each experimental condition were resolved and probed by SDS-PAGE followed by Western blot, performed according to standard protocols. Incubation with the primary antibodies diluted in 0.5% milk TBS-Tween 20 (TBS-T) was performed for 1–2 h at RT or overnight at 4°C, using a mouse monoclonal anti-atx3 antibody (1H9, 1:1,000; Millipore), the rabbit polyclonal anti-Patx3 (1:20; production described under Generation of the anti-Patx3 phosphospecific antibody), a mouse monoclonal anti-actin (β; 1:5,000; Sigma-Aldrich), or a rabbit polyclonal anti-Ub (1:1,000; Dako). The appropriate alkaline phosphatase-conjugated secondary antibodies (goat anti–mouse IgG and mouse anti–rabbit IgG; Jackson ImmunoResearch Laboratories) diluted in 0.5% milk TBS-T (1:10,000) were incubated for 1 h at RT. In the case of the anti-Patx3 antibody, 5% low-fat dry milk TBS-T was used in every step instead.

Dendritic morphology analysis

Transfected cortical neurons (low density) with 14–15 DIV were fixed with 4% paraformaldehyde/4% sucrose in PBS for 15 min at RT, and coverslips were mounted with Fluorescence Mounting Medium (Dako). GFP-atx3–expressing neurons were imaged at RT using an Axiovert 200M microscope (CCD monochromatic digital Axiocam HRm camera; Axiovision software; Carl Zeiss) and a 20× air objective (LD-PlanNeofluar, 0.4 NA; Carl Zeiss), and tracing of the cell body and dendrites was drawn based on the GFP signal, using the Neurolucida software (MBF Bioscience). Sholl analysis and dendritic measurement was performed with the Neurolucida Explorer software (MBF Bioscience). Total dendritic length of the neurons was normalized to the mean total dendritic length of neurons transfected with GFP-atx3 28Q WT, in each independent experiment. For each individual experiment, cells were cultured and immunocytochemically processed on the same occasion. Dendritic morphology analysis was performed blindly to condition.

Synapse quantification

Low-density cultures were fixed asdescribed in the previous paragraph, permeabilized with 0.25% Triton X-100 in PBS and blocked with 10% BSA. Primary antibodies diluted in 3% BSA PBS were incubated overnight at 4°C: the mouse monoclonal anti–PSD-95 (1:200; Affinity BioReagents), the guinea pig polyclonal anti-VGLUT1 (1:100,000; Millipore), and the mouse monoclonal anti-gephyrin (1:1,000; Synaptic Systems). Coverslips were then incubated with the secondary antibodies for 45 min at 37°C: Alexa Fluor 568 anti–mouse IgG (1:500; Invitrogen) and the Alexa Fluor 647 anti–guinea pig IgG (1:500; Molecular Probes). Coverslips were mounted with Fluorescence Mounting Medium.

Puncta observation and imaging was performed at RT with an Axio Observer Z1 microscope (CCD digital Axiocam HRm camera; ZEN Blue software; Carl Zeiss) with a 63× oil objective (Plan-Apochromat, 1.4 NA), after randomly selecting dendritic tracts (minimum 10 µm) in GFP-atx3–expressing neurons. Image analysis was performed using Fiji software (Schindelin et al., 2012) in manually thresholded images. Instances of colocalization of pre- and postsynaptic markers were quantified as functional synapses. Values were normalized per dendritic section length to the mean value of GFP-atx3 28Q WT in the respective experiment. For each individual experiment, cells were cultured and immunocytochemically processed on the same occasion, and images were acquired with the same settings. Synapse quantification was performed blindly to condition.

Quantification of aggregate-containing neurons

Transfected cortical neurons (medium-density cultures) with 8 DIV were fixed as described for the dendritic morpholoy analysis. Counting of GFP-atx3 aggregate-containing neurons was performed blindly to condition by manually scanning coverslips and observing the GFP fluorescence with a Zeiss Axiovert 200M microscope using a 63× oil objective (Plan-Apochromat, 1.4 NA). Aggregation was expressed as the fraction of cells with aggregates, normalized to the values obtained upon transfection with GFP-atx3 84Q WT, in each experiment.

In vivo lentiviral injections and MJD rat model generation

Adult male Wistar rats (Charles River Laboratories) were anesthetized and stereotaxically injected for delivery of lentiviral vectors to the striatum, following the procedure previously described in Alves et al. (2008b). For each animal, particles (400,000 ng of p24 antigen, 2 µl, 0.2 µl/min) encoding atx3 72Q WT were injected in the left hemisphere and particles encoding atx3 72Q S12D or S12A were injected in the right hemisphere.

Animals were housed in a temperature-controlled room and maintained on a 12-h light/dark cycle. Food and water were supplied ad libitum, and proceedings were executed in accordance with European Union Directive 2010/63/EW.

Rat striatum sample preparation and RT-PCR

Four weeks after injection, animals were terminally anesthetized with 80 mg/kg sodium pentobarbital (i.p.), brains were dissected fresh, and striatal punches were collected with a Harris Uni-Core pen (2.0-mm diameter; Ted Pella). Samples were kept frozen at –80°C.

Tissue punches were thawed at RT, and RNA extraction was performed using the QIAzolTM lysis reagent and the RNeasy Mini kit (QIAGEN), according to the recommended procedure. RNA concentration and purity were determined using the NanoDrop 2000 equipment (Thermo Fisher Scientific). cDNA synthesis was performed using the iScript cDNA Synthesis kit (Bio-Rad) from 1 mg of total RNA according to the manufacturer's instructions, and RT-PCR was performed with the SsoAdvanced SYBR Green Supermix kit (Bio-Rad) using predesigned primers (QuantiTect Primer Assays; QIAGEN): human atx3 (QT00094927) and human hypoxanthine-guanine phosphoribosyltransferase (QT00059066), used as housekeeping gene. 4 µl of cDNA diluted 100-fold with DNase free deionized water were used. PCR procedure consisted of one cycle at 95°C for 30 s, followed by 45 cycles of two steps: first at 95°C for 5 s, followed by 15 s at 55°C. The melting curve protocol started immediately after the quantitative PCR and consisted of 5 s at 65°C, with a 0.5°C temperature increase in each step until 95°C was reached. Threshold cycle values were generated automatically by the StepOne Software (Applied Biosystems). Standard curves were generated, and quantitative PCR efficiency was determined by the software. Relative quantification of mRNA levels with respect to control samples was determined by the Pfaffl method, taking into consideration the different amplification efficiencies of all genes.

Immunohistochemical processing

Four weeks after injection, animals were terminally anesthetized with 80 mg/kg sodium pentobarbital (i.p.) and transcardially perfused with 4% paraformaldehyde in PBS, pH 7. Whole brains were removed and incubated for 48 h in 20% sucrose PBS. Tissue was then frozen at –80°C, and 25-µm coronal sections of the striatal region were prepared using a cryostat-microtome (CM3050S; Leica). Slices were stored at 4°C, free-floating in 0.02% sodium azide PBS until further use.

Immunohistochemical quantitative analysis of atx3 accumulation and DARPP-32 depletion

On the occasion of immunohistochemical labeling, endogenous peroxidase activity of the slices was inhibited by incubating them with 0.1% phenylhydrazine in PBS for 30 min at 37°C. Slices were blocked with 10% normal goat serum, diluted in 0.1% Triton X-100 PBS for 1–2 h at RT and then incubated with the primary antibodies, diluted in blocking solution, overnight at 4°C: with the mouse monoclonal anti-atx3 antibody (1:4,000) or the rabbit polyclonal anti-DARPP-32 antibody (1:5,000; Chemicom). The suitable biotinylated secondary antibody (1:200; Vector Laboratories) diluted in blocking solution was incubated at RT for 2 h, and signal was developed by incubating slices with the VECTASTAIN Elite Avidin-Biotin-Peroxidase kit (Vector Laboratories) at RT, for 30–40 min, and then with the 3.3′-diaminobenzidine Peroxidase Substrate kit (Vector Laboratories). Sections were mounted, dehydrated, and finally coverslipped using the Eukitt mounting medium (O. Kindler).

Slices were analyzed and imaged at RT with an Axiovert 200M microscope (CCD color digital Axiocam HRc camera; Carl Zeiss), at 5× (air objective, Fluar, 0.25 NA) and 20× magnifications (air objective, LD-PlanNeofluar, 0.4 NA). Composite images of complete aggregate-containing or DARPP-32–depleted regions were automatically acquired using the MozaiX function of the AxioVision software.

Quantification of atx3-positive aggregates and determination of the area of the DARPP-32 depletion was made in 7–11 slices for each animal, spread over the anterior-posterior extent of the striatum and separated by 175 µm. Counting of atx3-positive aggregates was performed on 20×-magnified images of each hemisphere using ImageJ (National Institutes of Health). After manually thresholding images so that the recognizable atx3-positive accumulations were included in the examination, particles >3 μm^2 were automatically analyzed and counted (scale: 2 pixels/µm), and the estimative calculation of the total number of aggregates in the entire striatum was performed as previously described (Alves et al., 2008b). When comparing the quantity of aggregates between the two hemispheres, two percentages were calculated for each animal brain, representing the total number of aggregates in one hemisphere as a ratio of the total number of aggregates in the two hemispheres.

Determination of the area of the DARPP-32–depleted regions in the two hemispheres of each slice was performed on 5× images, using ImageJ to manually define the regions with decreased antibody reactivity and quantify their area (scale: 0.5 pixels/µm). Total depleted volume was estimated as previously described (Alves et al., 2008a). When comparing the volume of the DARPP-32–depleted region between the two hemispheres, two percentages were calculated for each animal brain, representing the total volume in one hemisphere as a ratio of the sum of the volumes from the two hemispheres.

In both cases, imaging, measurements, and quantifications were performed blindly to the hemisphere side.

Immunofluorescence staining of tissue sections and quantitative analysis of synaptic markers

Striatal slices were blocked for 1 h with 10% normal goat serum diluted in 0.2% Triton X-100 PBS and then incubated at 4°C for 72 h with the rabbit monoclonal anti–PSD-95 antibody (1:1,000; Cell Signaling Technology), the guinea pig polyclonal anti-VGLUT1 antibody (1:1,000; Millipore), and the mouse monoclonal anti-Myc tag antibody (clone 4A6; 1:1,000; Millipore), diluted in blocking solution. Sections were incubated overnight with secondary antibodies Alexa Fluor 488 anti–mouse IgG, Alexa Fluor 568 anti–rabbit IgG, and Alexa Fluor 647 anti–guinea pig IgG (1:500; Life Technologies) diluted in blocking solution, and finally mounted and coverslipped using Mowiol 4–88 (Sigma-Aldrich).

Slices were analyzed at RT with a confocal microscope (LSM 710; Carl Zeiss) using a 63× oil objective (Plan-Apochromat, 1.4 NA; QUASAR detection unit; ZEN Black software). Three-plane confocal images (0.053 × 0.053 × 0.67-μm^3 voxel size) of regions with homogenous punctuate PSD-95 and VGLUT1 signal were acquired in the vicinity of Myc-positive cell bodies from 10–11 slices spread over the anterior-posterior extent of the striatum and separated by 175 µm. 5–12 images were sampled in each hemisphere of each Myc-positive slice. Digital image deconvolution was performed using Huygens Essential (Scientific Volume Imaging).

Mean integrated density of PSD-95 and VGLUT-1 signals was determined at all possible thresholds and divided by total image area using an in-house–made macro for the Fiji software (Schindelin et al., 2012). The custom macro used to determine the mean integrated density of PSD-95 and VGLUT-1 signals at different thresholds is available in the online supplemental material.

Imaging, measurements, and quantifications were performed blindly to the hemisphere side.

Nuclear fractionation

Cells were washed with cold PBS and scraped onto buffer 1 (100 mM Hepes, 10 mM NaCl, 3 mM $MgCl_2$, 0.1% Triton X-100, and 1 mM EGTA, pH 7.5) supplemented with 1 mM, 1 mM PMSF, and 10 µg/ml CLAP. Extracts were incubated 40 min at 4°C and then centrifuged (2.400 *g*, 10 min, 4°C), supernatants were collected (cytoplasmic fraction), and pellets (nuclei) were resuspended in buffer 2 (25 mM Hepes, 300 mM NaCl, 5 mM $MgCl_2$, 1 mM EGTA, and 20% glycerol,

pH 7.4) supplemented with 1 mM PMSF and 10 µg/ml CLAP. After freeze-thawing the nuclei samples three times, they were incubated 1 h at 4°C and then centrifuged (12.000 *g*, 20 min, 4°C), and supernatants (nuclear fraction) were collected.

Cytosolic and nuclear fractions were denatured with 5× loading buffer and heated, and 40 µg of each sample was analyzed by Western blot as described using a mouse monoclonal anti-FLAG antibody (M2, 1:1,000; Sigma-Aldrich). Lamin enrichment of nuclear fractions was confirmed on rabbit polyclonal anti-lamin A antibody labeling (1:1,000; Sigma-Aldrich). Densitometric analysis of Western blot FLAG-atx3 protein bands was performed using ImageJ. Levels of nuclear FLAG-atx3 were expressed as the intensity of the nuclear protein bands, normalized to the sum of the intensity of these bands and the bands of the respective cytosolic fractions.

Statistical analysis

Statistical analysis was performed using the GraphPad Prism 5 software (GraphPad Software). Comparison between two conditions used the *t* test (two-tailed) when the values of both samples presented a Gaussian distribution or the Mann-Whitney test (two-tailed) in the cases where values did not display a normal distribution. Normality was assessed through the D'Agostino and Pearson omnibus normality test. Comparison of samples with a defined value (100%) used the one-sample *t* test. Comparison between more than two conditions was achieved with the Kruskal-Wallis test, whereas multiple comparisons were performed with two-way analysis of variance, followed by Bonferroni post hoc tests.

Online supplemental material

Fig. S1 shows the analysis of dendritic morphology and synapse number in cultured rat cortical neurons transfected with GFP-atx3 28Q WT and the corresponding empty vector. The Western blot represented in Fig. S2 evidences the levels of GFP-atx3 28Q and 84Q WT and the S12 phosphomutants in transfected cortical neurons. Fig. S3 compares the percentage of aggregate-displaying neurons between cultures transfected with GFP-atx3 28Q and 84Q WT and the respective DUB inactive C14A mutants. The RT-PCR analysis of atx3 72Q expression levels in each lentiviral model rat brain hemisphere is shown in Fig. S4. Fig. S5 compares FLAG-atx3 nuclear levels between COS-7 cell samples transfected with FLAG-atx3 WT and the S12 phosphomutants. Thresholderer is an ImageJ macro developed to analyze different immunofluorescence microscopy image parameters, including integrated signal density, at consecutive threshold levels. The source code for Thresholderer is provided in the online supplemental material. Online supplemental material is available at http://www.jcb.org/cgi/content/full/jcb.201506025/DC1.

Acknowledgments

We thank P. Maciel for critical reading of the manuscript. We thank M. Laço, J. Santos, V. Anjos, G. Caldeira, and I. Salazar for technical help, E. Carvalho for assistance in the preparation of cultured neurons, and I. Onofre and D. Pereira for contributing the human fibroblast lines used.

This study was supported by national funds through the Portuguese Science and Technology Foundation and by the European Union - European Fund for Economic and Regional Develoment funding through the Operational Competitiveness Program (COMPETE; grants PTDC/SAU-NMC/110602/2009, PEst-C/SAU/LA0001/2013-2014, and UID/NEU/04539/2013), through Programa Operacional Regional do Norte (ON.2 - O Novo Norte), under Quadro de Referência Estratégico Nacional (grants NORTE-07-0124-000001—Neurodegenerative Diseases), and by Programa Mais Centro (CENTRO-07-ST24-FEDER-002002, 002006, 002008). C.A. Matos and B. Almeida were supported by the Portuguese Science and Technology Foundation through Fellowship SFRH/BD/47160/2008 and SFRH/BPD/70783/2010, respectively.

The authors declare no competing financial interests.

Submitted: 4 June 2015
Accepted: 19 January 2016

References

Aiken, C.T., J.S.Steffan, C.M.Guerrero, H.Khashwji, T.Lukacsovich, D.Simmons, J.M.Purcell, K.Menhaji, Y.Z.Zhu, K.Green, et al.2009. Phosphorylation of threonine 3: implications for Huntingtin aggregation and neurotoxicity. *J. Biol. Chem.*284:29427–29436. http://dx.doi.org/10.1074/jbc.M109.013193

Almeida, B., S.Fernandes, I.A.Abreu, and S.Macedo-Ribeiro. 2013. Trinucleotide repeats: a structural perspective. *Front. Neurol.*4:76. http://dx.doi.org/10.3389/fneur.2013.00076

Alves, S., I.Nascimento-Ferreira, G.Auregan, R.Hassig, N.Dufour, E.Brouillet, M.C.Pedroso de Lima, P.Hantraye, L.Pereira de Almeida, and N.Déglon. 2008a. Allele-specific RNA silencing of mutant ataxin-3 mediates neuroprotection in a rat model of Machado-Joseph disease. *PLoS One.*3:e3341. http://dx.doi.org/10.1371/journal.pone.0003341

Alves, S., E.Régulier, I.Nascimento-Ferreira, R.Hassig, N.Dufour, A.Koeppen, A.L.Carvalho, S.Simões, M.C.de Lima, E.Brouillet, et al.2008b. Striatal and nigral pathology in a lentiviral rat model of Machado-Joseph disease. *Hum. Mol. Genet.*17:2071–2083. http://dx.doi.org/10.1093/hmg/ddn106

Alves, S., I.Nascimento-Ferreira, N.Dufour, R.Hassig, G.Auregan, C.Nóbrega, E.Brouillet, P.Hantraye, M.C.Pedroso de Lima, N.Déglon, and L.P.de Almeida. 2010. Silencing ataxin-3 mitigates degeneration in a rat model of Machado-Joseph disease: no role for wild-type ataxin-3?*Hum. Mol. Genet.*19:2380–2394. http://dx.doi.org/10.1093/hmg/ddq111

Bauer, P.O., and N.Nukina. 2009. The pathogenic mechanisms of polyglutamine diseases and current therapeutic strategies. *J. Neurochem.*110:1737–1765. http://dx.doi.org/10.1111/j.1471-4159.2009.06302.x

Berke, S.J., Y.Chai, G.L.Marrs, H.Wen, and H.L.Paulson. 2005. Defining the role of ubiquitin-interacting motifs in the polyglutamine disease protein, ataxin-3. *J. Biol. Chem.*280:32026–32034. http://dx.doi.org/10.1074/jbc.M506084200

Bettencourt, C., and M.Lima. 2011. Machado-Joseph Disease: from first descriptions to new perspectives. *Orphanet J. Rare Dis.*6:35. http://dx.doi.org/10.1186/1750-1172-6-35

Boy, J., T.Schmidt, U.Schumann, U.Grasshoff, S.Unser, C.Holzmann, I.Schmitt, T.Karl, F.Laccone, H.Wolburg, et al.2010. A transgenic mouse model of spinocerebellar ataxia type 3 resembling late disease onset and gender-specific instability of CAG repeats. *Neurobiol. Dis.*37:284–293. http://dx.doi.org/10.1016/j.nbd.2009.08.002

Burnett, B., F.Li, and R.N.Pittman. 2003. The polyglutamine neurodegenerative protein ataxin-3 binds polyubiquitylated proteins and has ubiquitin protease activity. *Hum. Mol. Genet.*12:3195–3205. http://dx.doi.org/10.1093/hmg/ddg344

Chai, Y., S.L.Koppenhafer, S.J.Shoesmith, M.K.Perez, and H.L.Paulson. 1999. Evidence for proteasome involvement in polyglutamine disease: localization to nuclear inclusions in SCA3/MJD and suppression of polyglutamine aggregation in vitro. *Hum. Mol. Genet.*8:673–682. http://dx.doi.org/10.1093/hmg/8.4.673

Chou, A.H., T.H.Yeh, P.Ouyang, Y.L.Chen, S.Y.Chen, and H.L.Wang. 2008. Polyglutamine-expanded ataxin-3 causes cerebellar dysfunction of SCA 3 transgenic mice by inducing transcriptional dysregulation. *Neurobiol. Dis.*31:89–101. http://dx.doi.org/10.1016/j.nbd.2008.03.011

D'Abreu, A., M.C.FrançaJr., C.L.Yasuda, B.A.Campos, I.Lopes-Cendes, and F.Cendes. 2012. Neocortical atrophy in Machado-Joseph disease: a longitudinal neuroimaging study. *J. Neuroimaging.*22:285–291. http://dx.doi.org/10.1111/j.1552-6569.2011.00614.x

de Almeida, L.P., C.A.Ross, D.Zala, P.Aebischer, and N.Déglon. 2002. Lentiviral-mediated delivery of mutant huntingtin in the striatum of rats induces a selective neuropathology modulated by polyglutamine repeat size, huntingtin expression levels, and protein length. *J. Neurosci.*22:3473–3483.

Ellisdon, A.M., B.Thomas, and S.P.Bottomley. 2006. The two-stage pathway of ataxin-3 fibrillogenesis involves a polyglutamine-independent

step. *J. Biol. Chem.*281:16888–16896. http://dx.doi.org/10.1074/jbc.M601470200

Emamian, E.S., M.D.Kaytor, L.A.Duvick, T.Zu, S.K.Tousey, H.Y.Zoghbi, H.B.Clark, and H.T.Orr. 2003. Serine 776 of ataxin-1 is critical for polyglutamine-induced disease in SCA1 transgenic mice. *Neuron.*38:375–387. http://dx.doi.org/10.1016/S0896-6273(03)00258-7

Fei, E., N.Jia, T.Zhang, X.Ma, H.Wang, C.Liu, W.Zhang, L.Ding, N.Nukina, and G.Wang. 2007. Phosphorylation of ataxin-3 by glycogen synthase kinase 3beta at serine 256 regulates the aggregation of ataxin-3. *Biochem. Biophys. Res. Commun.*357:487–492. http://dx.doi.org/10.1016/j.bbrc.2007.03.160

Gales, L., L.Cortes, C.Almeida, C.V.Melo, M.C.Costa, P.Maciel, D.T.Clarke, A.M.Damas, and S.Macedo-Ribeiro. 2005. Towards a structural understanding of the fibrillization pathway in Machado-Joseph's disease: trapping early oligomers of non-expanded ataxin-3. *J. Mol. Biol.*353:642–654. http://dx.doi.org/10.1016/j.jmb.2005.08.061

Gatchel, J.R., and H.Y.Zoghbi. 2005. Diseases of unstable repeat expansion: mechanisms and common principles. *Nat. Rev. Genet.*6:743–755. http://dx.doi.org/10.1038/nrg1691

Harris, G.M., K.Dodelzon, L.Gong, P.Gonzalez-Alegre, and H.L.Paulson. 2010. Splice isoforms of the polyglutamine disease protein ataxin-3 exhibit similar enzymatic yet different aggregation properties. *PLoS One.*5:e13695. http://dx.doi.org/10.1371/journal.pone.0013695

Huang, O.W., X.Ma, J.Yin, J.Flinders, T.Maurer, N.Kayagaki, Q.Phung, I.Bosanac, D.Arnott, V.M.Dixit, et al.2012. Phosphorylation-dependent activity of the deubiquitinase DUBA. *Nat. Struct. Mol. Biol.*19:171–175. http://dx.doi.org/10.1038/nsmb.2206

Humbert, S., E.A.Bryson, F.P.Cordelières, N.C.Connors, S.R.Datta, S.Finkbeiner, M.E.Greenberg, and F.Saudou. 2002. The IGF-1/Akt pathway is neuroprotective in Huntington's disease and involves Huntingtin phosphorylation by Akt. *Dev. Cell.*2:831–837. http://dx.doi.org/10.1016/S1534-5807(02)00188-0

Hunter, T.2007. The age of crosstalk: phosphorylation, ubiquitination, and beyond. *Mol. Cell.*28:730–738. http://dx.doi.org/10.1016/j.molcel.2007.11.019

Ichikawa, Y., J.Goto, M.Hattori, A.Toyoda, K.Ishii, S.Y.Jeong, H.Hashida, N.Masuda, K.Ogata, F.Kasai, et al.2001. The genomic structure and expression of MJD, the Machado-Joseph disease gene. *J. Hum. Genet.*46:413–422. http://dx.doi.org/10.1007/s100380170060

Ishikawa, A., M.Yamada, K.Makino, I.Aida, J.Idezuka, T.Ikeuchi, Y.Soma, H.Takahashi, and S.Tsuji. 2002. Dementia and delirium in 4 patients with Machado-Joseph disease. *Arch. Neurol.*59:1804–1808. http://dx.doi.org/10.1001/archneur.59.11.1804

Jiang, M., L.Deng, and G.Chen. 2004. High Ca(2+)-phosphate transfection efficiency enables single neuron gene analysis. *Gene Ther.*11:1303–1311. http://dx.doi.org/10.1038/sj.gt.3302305

Kawaguchi, Y., T.Okamoto, M.Taniwaki, M.Aizawa, M.Inoue, S.Katayama, H.Kawakami, S.Nakamura, M.Nishimura, I.Akiguchi, et al.1994. CAG expansions in a novel gene for Machado-Joseph disease at chromosome 14q32.1. *Nat. Genet.*8:221–228. http://dx.doi.org/10.1038/ng1194-221

Koch, P., P.Breuer, M.Peitz, J.Jungverdorben, J.Kesavan, D.Poppe, J.Doerr, J.Ladewig, J.Mertens, T.Tüting, et al.. 2011. Excitation-induced ataxin-3 aggregation in neurons from patients with Machado-Joseph disease. *Nature.*480:543–546. http://dx.doi.org/10.1038/nature10671

Komander, D., M.J.Clague, and S.Urbé. 2009. Breaking the chains: structure and function of the deubiquitinases. *Nat. Rev. Mol. Cell Biol.*10:550–563. http://dx.doi.org/10.1038/nrm2731

Konno, A., A.N.Shuvaev, N.Miyake, K.Miyake, A.Iizuka, S.Matsuura, F.Huda, K.Nakamura, S.Yanagi, T.Shimada, and H.Hirai. 2014. Mutant ataxin-3 with an abnormally expanded polyglutamine chain disrupts dendritic development and metabotropic glutamate receptor signaling in mouse cerebellar Purkinje cells. *Cerebellum.*13:29–41. http://dx.doi.org/10.1007/s12311-013-0516-5

La Spada, A.R., and J.P.Taylor. 2010. Repeat expansion disease: progress and puzzles in disease pathogenesis. *Nat. Rev. Genet.*11:247–258. http://dx.doi.org/10.1038/nrg2748

Lee, S.B., J.A.Bagley, H.Y.Lee, L.Y.Jan, and Y.N.Jan. 2011. Pathogenic polyglutamine proteins cause dendrite defects associated with specific actin cytoskeletal alterations in Drosophila. *Proc. Natl. Acad. Sci. USA.*108:16795–16800. http://dx.doi.org/10.1073/pnas.1113573108

Lopes, T.M., A.D'Abreu, M.C.FrançaJr., C.L.Yasuda, L.E.Betting, A.B.Samara, G.Castellano, J.C.Somazz, M.L.Balthazar, I.Lopes-Cendes, and F.Cendes. 2013. Widespread neuronal damage and cognitive dysfunction in spinocerebellar ataxia type 3. *J. Neurol.*260:2370–2379. http://dx.doi.org/10.1007/s00415-013-6998-8

Luo, S., C.Vacher, J.E.Davies, and D.C.Rubinsztein. 2005. Cdk5 phosphorylation of huntingtin reduces its cleavage by caspases: implications for mutant huntingtin toxicity. *J. Cell Biol.*169:647–656. http://dx.doi.org/10.1083/jcb.200412071

Mao, Y., F.Senic-Matuglia, P.P.Di Fiore, S.Polo, M.E.Hodsdon, and P.De Camilli. 2005. Deubiquitinating function of ataxin-3: insights from the solution structure of the Josephin domain. *Proc. Natl. Acad. Sci. USA.*102:12700–12705. http://dx.doi.org/10.1073/pnas.0506344102

Masino, L., V.Musi, R.P.Menon, P.Fusi, G.Kelly, T.A.Frenkiel, Y.Trottier, and A.Pastore. 2003. Domain architecture of the polyglutamine protein ataxin-3: a globular domain followed by a flexible tail. *FEBS Lett.*549:21–25. http://dx.doi.org/10.1016/S0014-5793(03)00748-8

Masino, L., G.Nicastro, R.P.Menon, F.Dal Piaz, L.Calder, and A.Pastore. 2004. Characterization of the structure and the amyloidogenic properties of the Josephin domain of the polyglutamine-containing protein ataxin-3. *J. Mol. Biol.*344:1021–1035. http://dx.doi.org/10.1016/j.jmb.2004.09.065

Masino, L., G.Nicastro, L.Calder, M.Vendruscolo, and A.Pastore. 2011. Functional interactions as a survival strategy against abnormal aggregation. *FASEB J.*25:45–54. http://dx.doi.org/10.1096/fj.10-161208

Matos, C.A., S.de Macedo-Ribeiro, and A.L.Carvalho. 2011. Polyglutamine diseases: the special case of ataxin-3 and Machado-Joseph disease. *Prog. Neurobiol.*95:26–48. http://dx.doi.org/10.1016/j.pneurobio.2011.06.007

Mueller, T., P.Breuer, I.Schmitt, J.Walter, B.O.Evert, and U.Wüllner. 2009. CK2-dependent phosphorylation determines cellular localization and stability of ataxin-3. *Hum. Mol. Genet.*18:3334–3343. http://dx.doi.org/10.1093/hmg/ddp274

Murata, Y., S.Yamaguchi, H.Kawakami, Y.Imon, H.Maruyama, T.Sakai, T.Kazuta, T.Ohtake, M.Nishimura, T.Saida, et al.1998. Characteristic magnetic resonance imaging findings in Machado-Joseph disease. *Arch. Neurol.*55:33–37. http://dx.doi.org/10.1001/archneur.55.1.33

Nascimento-Ferreira, I., T.Santos-Ferreira, L.Sousa-Ferreira, G.Auregan, I.Onofre, S.Alves, N.Dufour, V.F.Colomer Gould, A.Koeppen, N.Déglon, and L.Pereira de Almeida. 2011. Overexpression of the autophagic beclin-1 protein clears mutant ataxin-3 and alleviates Machado-Joseph disease. *Brain.*134:1400–1415. http://dx.doi.org/10.1093/brain/awr047

Neves-Carvalho, A., E.Logarinho, A.Freitas, S.Duarte-Silva, M.C.Costa, A.Silva-Fernandes, M.Martins, S.C.Serra, A.T.Lopes, H.L.Paulson, et al.2015. Dominant negative effect of polyglutamine expansion perturbs normal function of ataxin-3 in neuronal cells. *Hum. Mol. Genet.*24:100–117. http://dx.doi.org/10.1093/hmg/ddu422

Nicastro, G., R.P.Menon, L.Masino, P.P.Knowles, N.Q.McDonald, and A.Pastore. 2005. The solution structure of the Josephin domain of ataxin-3: structural determinants for molecular recognition. *Proc. Natl. Acad. Sci. USA.*102:10493–10498. http://dx.doi.org/10.1073/pnas.0501732102

Nicastro, G., L.Masino, V.Esposito, R.P.Menon, A.De Simone, F.Fraternali, and A.Pastore. 2009. Josephin domain of ataxin-3 contains two distinct ubiquitin-binding sites. *Biopolymers.*91:1203–1214. http://dx.doi.org/10.1002/bip.21210

Pardo, R., E.Colin, E.Régulier, P.Aebischer, N.Déglon, S.Humbert, and F.Saudou. 2006. Inhibition of calcineurin by FK506 protects against polyglutamine-huntingtin toxicity through an increase of huntingtin phosphorylation at S421. *J. Neurosci.*26:1635–1645. http://dx.doi.org/10.1523/JNEUROSCI.3706-05.2006

Paulson, H.L., S.S.Das, P.B.Crino, M.K.Perez, S.C.Patel, D.Gotsdiner, K.H.Fischbeck, and R.N.Pittman. 1997a. Machado-Joseph disease gene product is a cytoplasmic protein widely expressed in brain. *Ann. Neurol.*41:453–462. http://dx.doi.org/10.1002/ana.410410408

Paulson, H.L., M.K.Perez, Y.Trottier, J.Q.Trojanowski, S.H.Subramony, S.S.Das, P.Vig, J.L.Mandel, K.H.Fischbeck, and R.N.Pittman. 1997b. Intranuclear inclusions of expanded polyglutamine protein in spinocerebellar ataxia type 3. *Neuron.*19:333–344. http://dx.doi.org/10.1016/S0896-6273(00)80943-5

Pedroso, J.L., M.C.FrançaJr., P.Braga-Neto, A.D'Abreu, M.L.Saraiva-Pereira, J.A.Saute, H.A.Teive, P.Caramelli, L.B.Jardim, I.Lopes-Cendes, and O.G.Barsottini. 2013. Nonmotor and extracerebellar features in Machado-Joseph disease: a review. *Mov. Disord.*28:1200–1208. http://dx.doi.org/10.1002/mds.25513

Pennuto, M., I.Palazzolo, and A.Poletti. 2009. Post-translational modifications of expanded polyglutamine proteins: impact on neurotoxicity. *Hum. Mol. Genet.*18(R1):R40–R47. http://dx.doi.org/10.1093/hmg/ddn412

Pozzi, C., M.Valtorta, G.Tedeschi, E.Galbusera, V.Pastori, A.Bigi, S.Nonnis, E.Grassi, and P.Fusi. 2008. Study of subcellular localization and proteolysis of ataxin-3. *Neurobiol. Dis.*30:190–200. http://dx.doi.org/10.1016/j.nbd.2008.01.011

Renatus, M., and C.J.Farady. 2012. Phosphorylation meets proteolysis. *Structure.*20:570–571. http://dx.doi.org/10.1016/j.str.2012.03.006

Robert, X., and P.Gouet. 2014. Deciphering key features in protein structures with the new ENDscript server. *Nucleic Acids Res.*42(W1):W320–W324. http://dx.doi.org/10.1093/nar/gku316

Rodrigues, A.J., G.Coppola, C.Santos, M.C.Costa, M.Ailion, J.Sequeiros, D.H.Geschwind, and P.Maciel. 2007. Functional genomics and biochemical characterization of the C. elegans orthologue of the Machado-Joseph disease protein ataxin-3. *FASEB J.*21:1126–1136. http ://dx.doi.org/10.1096/fj.06-7002com

Rodrigues, A.J., M.do Carmo Costa, T.L.Silva, D.Ferreira, F.Bajanca, E.Logarinho, and P.Maciel. 2010. Absence of ataxin-3 leads to cytoskeletal disorganization and increased cell death. *Biochim. Biophys. Acta.*1803:1154–1163. http://dx.doi.org/10.1016/j.bbamcr.2010.07.004

Rüb, U., L.Schöls, H.Paulson, G.Auburger, P.Kermer, J.C.Jen, K.Seidel, H.W.Korf, and T.Deller. 2013. Clinical features, neurogenetics and neuropathology of the polyglutamine spinocerebellar ataxias type 1, 2, 3, 6 and 7. *Prog. Neurobiol.*104:38–66. http://dx.doi.org/10.1016/j .pneurobio.2013.01.001

Scarff, C.A., B.Almeida, J.Fraga, S.Macedo-Ribeiro, S.E.Radford, and A.E.Ashcroft. 2015. Examination of Ataxin-3 (atx-3) Aggregation by Structural Mass Spectrometry Techniques: A Rationale for Expedited Aggregation upon Polyglutamine (polyQ) Expansion. *Mol. Cell. Proteomics.*14:1241–1253. http://dx.doi.org/10.1074/mcp.M114.044610

Schindelin, J., I.Arganda-Carreras, E.Frise, V.Kaynig, M.Longair, T.Pietzsch, S.Preibisch, C.Rueden, S.Saalfeld, B.Schmid, et al.2012. Fiji: an open-source platform for biological-image analysis. *Nat. Methods.*9:676–682. http://dx.doi.org/10.1038/nmeth.2019

Schöls, L., P.Bauer, T.Schmidt, T.Schulte, and O.Riess. 2004. Autosomal dominant cerebellar ataxias: clinical features, genetics, and pathogenesis. *Lancet Neurol.*3:291–304. http://dx.doi.org/10.1016/S1474 -4422(04)00737-9

Shakkottai, V.G., M.do Carmo Costa, J.M.Dell'Orco, A.Sankaranarayanan, H.Wulff, and H.L.Paulson. 2011. Early changes in cerebellar physiology accompany motor dysfunction in the polyglutamine disease spinocerebellar ataxia type 3. *J. Neurosci.*31:13002–13014. http://dx.doi .org/10.1523/JNEUROSCI.2789-11.2011

Simões, A.T., N.Gonçalves, A.Koeppen, N.Déglon, S.Kügler, C.B.Duarte, and L.Pereira de Almeida. 2012. Calpastatin-mediated inhibition of calpains in the mouse brain prevents mutant ataxin 3 proteolysis, nuclear localization and aggregation, relieving Machado-Joseph disease. *Brain.*135:2428–2439. http://dx.doi.org/10.1093/brain/aws177

Song, A.X., C.J.Zhou, Y.Peng, X.C.Gao, Z.R.Zhou, Q.S.Fu, J.Hong, D.H.Lin, and H.Y.Hu. 2010. Structural transformation of the tandem ubiquitin-interacting motifs in ataxin-3 and their cooperative interactions with ubiquitin chains. *PLoS One.*5:e13202. http://dx.doi.org/10.1371/journal .pone.0013202

Soong, B., C.Cheng, R.Liu, and D.Shan. 1997. Machado-Joseph disease: clinical, molecular, and metabolic characterization in Chinese kindreds. *Ann. Neurol.*41:446–452. http://dx.doi.org/10.1002/ana.410410407

Takahashi, T., S.Katada, and O.Onodera. 2010. Polyglutamine diseases: where does toxicity come from? what is toxicity? where are we going?*J. Mol. Cell Biol.*2:180–191. http://dx.doi.org/10.1093/jmcb/mjq005

Taniwaki, T., T.Sakai, T.Kobayashi, Y.Kuwabara, M.Otsuka, Y.Ichiya, K.Masuda, and I.Goto. 1997. Positron emission tomography (PET) in Machado-Joseph disease. *J. Neurol. Sci.*145:63–67. http://dx.doi.org/10.1016/ S0022-510X(96)00242-0

Tao, R.S., E.K.Fei, Z.Ying, H.F.Wang, and G.H.Wang. 2008. Casein kinase 2 interacts with and phosphorylates ataxin-3. *Neurosci. Bull.*24:271–277. http://dx.doi.org/10.1007/s12264-008-0605-5

Tarrant, M.K., and P.A.Cole. 2009. The chemical biology of protein phosphorylation. *Annu. Rev. Biochem.*78:797–825. http://dx.doi.org/10 .1146/annurev.biochem.78.070907.103047

Todi, S.V., K.M.Scaglione, J.R.Blount, V.Basrur, K.P.Conlon, A.Pastore, K.Elenitoba-Johnson, and H.L.Paulson. 2010. Activity and cellular functions of the deubiquitinating enzyme and polyglutamine disease protein ataxin-3 are regulated by ubiquitination at lysine 117. *J. Biol. Chem.*285:39303–39313. http://dx.doi.org/10.1074/jbc.M110.181610

Trottier, Y., G.Cancel, I.An-Gourfinkel, Y.Lutz, C.Weber, A.Brice, E.Hirsch, and J.L.Mandel. 1998. Heterogeneous intracellular localization and expression of ataxin-3. *Neurobiol. Dis.*5:335–347. http://dx.doi.org/10 .1006/nbdi.1998.0208

Weeks, S.D., K.C.Grasty, L.Hernandez-Cuebas, and P.J.Loll. 2011. Crystal structure of a Josephin-ubiquitin complex: evolutionary restraints on ataxin-3 deubiquitinating activity. *J. Biol. Chem.*286:4555–4565. http:// dx.doi.org/10.1074/jbc.M110.177360

Yamada, M., S.Hayashi, S.Tsuji, and H.Takahashi. 2001. Involvement of the cerebral cortex and autonomic ganglia in Machado-Joseph disease. *Acta Neuropathol.*101:140–144.

Zoghbi, H.Y., and H.T.Orr. 2000. Glutamine repeats and neurodegeneration. *Annu. Rev. Neurosci.*23:217–247. http://dx.doi.org/10.1146/annurev.neuro.23.1.217

Matos et al., http://www.jcb.org/cgi/content/full/jcb.201506025/DC1

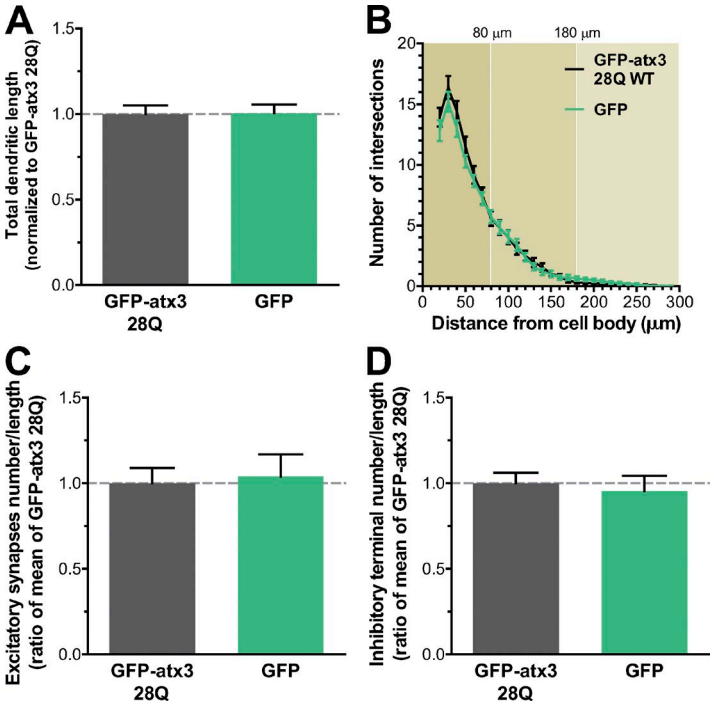

Figure S1. **Nonexpanded GFP-atx3 causes no neuromorphologic anomalies in transiently transfected cortical neurons.** Rat cortical neuron cultures were transfected with GFP-atx3 28Q or the empty pEGFP-C1 vector (GFP). (A) Neurons expressing GFP-atx3 28Q WT display no differences regarding total dendritic length (n = 42–47 neurons, from four independent experiments; t test: $P > 0.9$) or the dendritic arborization profile (B) as evaluated by Sholl analysis (n = 42–47 neurons, from four independent experiments; t test: $P > 0.05$). (C) No differences relative to the number of excitatory synapses (n = 38–40 neurons, from four independent experiments; t test: $P > 0.8$) or (D) inhibitory postsynaptic terminals (n = 35–34 neurons, from three independent experiments; t test: $P > 0.6$), were detected. (A–D) Graph bars represent mean ± SEM.

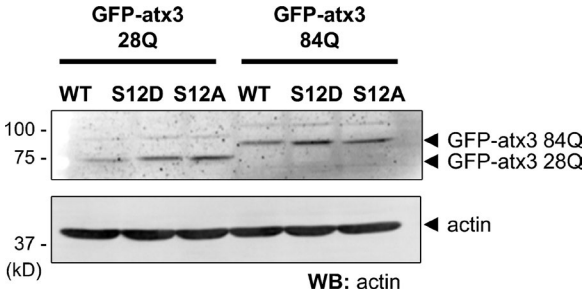

Figure S2. **Transfection of rat cortical neurons with GFP-atx3 phosphomutants.** Cultured rat cortical neurons with 9–10 DIV were transfected with GFP-atx3 28Q WT, GFP-atx3 84Q WT, or the respective S12D or S12A mutants, and 5 d later whole-cell lysates were analyzed by Western blot with an anti-GFP and an antiactin antibody. The differences in electrophoretic movement between GFP-atx3 28Q and GFP-atx3 84Q reflect the differences in molecular size resulting from the distinct number of glutamine residues.

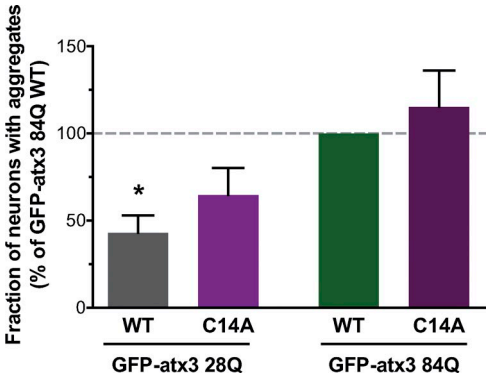

Figure S3. **DUB activity blocking causes no change on expanded atx3 aggregation in cortical neurons.** Transfection with the DUB inactive mutant GFP -atx3 84Q C14A yields a fraction of neurons with aggregates comparable with what is obtained on transfection with GFP-atx3 84Q WT (50–55 neurons counted for each condition in $n = 7$ independently prepared cultures; graph bars represent mean ± SEM; one-sample t test: *, $P < 0.05$).

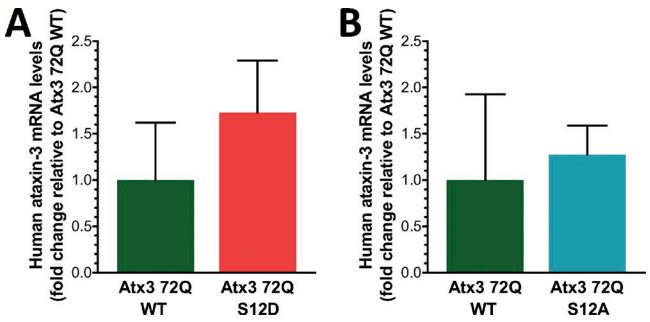

Figure S4. **Expression levels of atx3 72Q in the striatum of the MJD lentiviral rat models.** (A and B) RT-PCR analysis of human atx3 mRNA levels revealed no significant differences between brain hemispheres ($n = 3$ animals injected with atx3 72Q WT:atx3 72Q S12D or atx3 72Q WT:atx3 72Q S12A; graph bars represent mean ± SEM; Mann-Whitney test: $P > 0.05$).

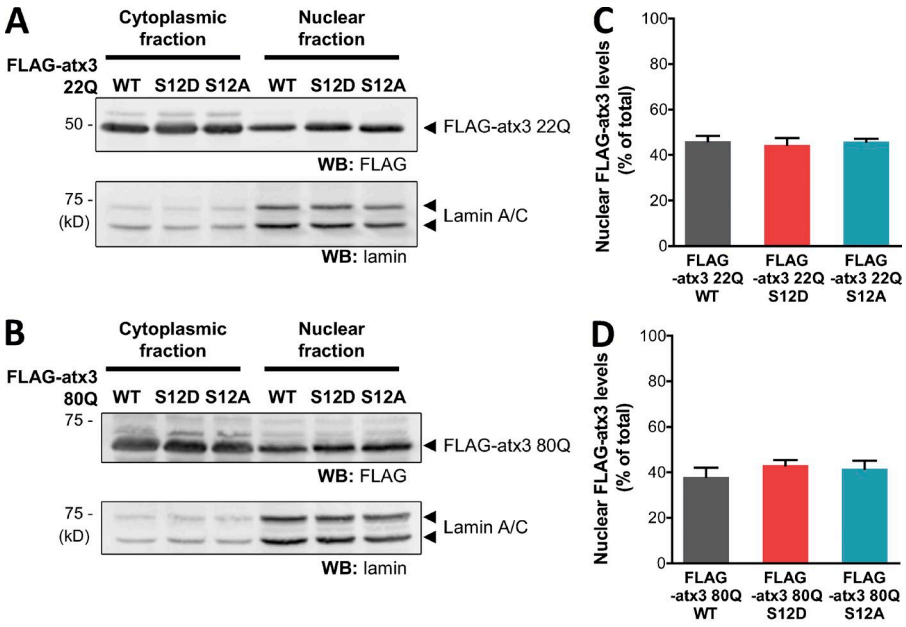

Figure S5. **Mutating S12 does not alter the nuclear accumulation of atx3, in COS-7 cells.** (A and B) COS-7 cells were transiently transfected with nonexpanded (22Q) or expanded (80Q) forms of WT and phosphomutated FLAG-atx3. Cell extracts were subjected to a nuclear fractionation procedure and the resulting cytoplasmic and nuclear fractions were analyzed by Western blot to evaluate the relative abundance of FLAG-atx3. Enrichment of lamin in the nuclear fractions was used as a control for the fractionation procedure. (C and D) For both expanded and nonexpanded forms of FLAG-atx3, densitometric analysis of the blots revealed that the phosphomutants have the same tendency for nuclear accumulation as their nonmutated counterparts (FLAG-atx3 22Q: $n = 3$ independent experiments; FLAG-atx3 84Q: five independent experiments; graph bars represent mean ± SEM; Kruskal-Wallis test: $P > 0.05$).

Provided online is the source code for Thresholderer, an ImageJ macro developed to analyze different immunofluorescence microscopy image parameters, including integrated signal density, at consecutive threshold levels.